Bridging the 3D geometrical organisation of white matter pathways across anatomical length scales and species

Hans Martin Kjer (1,2), Mariam Andersson (1,2), Yi He (1,3), Alexandra Pacureanu (4), Alessandro Daducci (5), Marco Pizzolato (2), Tim Salditt (7), Anna-Lena Robisch (7), Marina Eckermann (7,4), Mareike Toepperwien (7), Anders Bjorholm Dahl (2), Maria Louise Elkjær (8, 9), Zsolt Illes (8,9,10,11), Maurice Ptito (12,13), Vedrana Andersen Dahl (2), Tim B. Dyrby (1,2)

1. Danish Research Centre for Magnetic Resonance, Center for Functional and Diagnostic Imaging and Research, Copenhagen University Hospital Amager and Hvidovre, 2650 Hvidovre, Denmark
2. Department of Applied Mathematics and Computer Science, Technical University of Denmark, 2800 Kongens Lyngby, Denmark
3. Guangdong Provincial Engineering Research Center of Molecular Imaging, The Fifth Affiliated Hospital, Sun Yat-sen University, 519000 Zhuhai, China
4. ESRF - The European Synchrotron, 38043 Grenoble Cedex 9, France
5. Department of Computer Science, University of Verona, Verona, Italy
7. Institut für Röntgenphysik, Universität Göttingen, Friedrich-Hund-Platz. 1, D-37077 Göttingen, Germany
8. Department of Neurology, Odense University Hospital, 5000 Odense, Denmark
9. Institute of Molecular Medicine, University of Southern Denmark, Odense, Denmark
10. BRIDGE—Brain Research—Inter-Disciplinary Guided Excellence, Department of Clinical Research, University of Southern Denmark, 5000 Odense, Denmark
11. Rheumatology Research Unit, Odense University Hospital, 5000 Odense, Denmark
12. School of Optometry, University of Montreal, Montreal, Canada
13. Department of Neuroscience, Faculty of Health Science, University of Copenhagen, 2200 Copenhagen, Denmark

Corresponding authors:

Hans Martin Kjer, hmkj@dtu.dk
Tim B. Dyrby, timd@drcmr.dk

ABSTRACT
We used diffusion MRI and x-ray synchrotron imaging on monkey and mice brains to examine the organisation of fibre pathways in white matter across anatomical scales. We compared the structure in the corpus callosum and crossing fibre regions and investigated the differences in cuprizone-induced experimental demyelination mouse brains versus healthy controls. Our findings revealed common principles of fibre organisation in the two species; small axonal fasciculi and major bundles formed laminar structures with varying angles, according to the characteristics of major pathways. Individual axon fasciculi exhibited tortuous paths around obstacles like blood vessels, but in a manner independent of fibre complexity and demyelination. A quantitative analysis of tissue anisotropies and fibre orientation distributions gave consistent results for different anatomical length scales and modalities, while being dependent on the field-of-view. Our study emphasises the need to balance field-of-view and voxel size when characterising white matter features across anatomical length scales.

1. INTRODUCTION

The connectome is the map of axonal connections between different brain regions. Mapping of the connectome across several anatomical length scales can unravel its hierarchical organisation, which bears a close association with normal brain function and with disruptions in disease states. The major white matter pathways can be outlined at millimetre image resolution, e.g. through photographic microdissection or tractography on diffusion magnetic resonance imaging (dMRI)(*1*). They include the association, projection, and interhemispheric pathways, which are further categorised into functionally related tracts such as the pyramidal tract and the inferior fronto occipital fasciculus. At millimetre resolution, the white matter tracts appear to form a structural backbone, but examination at higher resolution shows a particular topological and spatial organisation of the axonal fasciculi within (*2*). The pyramidal tract, for example, has a topological organisation into parallel fasciculi determined by the homunculus organisation of the primary motor cortex. Hence, diseases such as amyotrophic lateral sclerosis that over time results in the loss of different types of motor control, correlate in the pyramidal tract with a topological dependent axonal degeneration (*3*).

The conventional model of white matter architecture has assumed a parallel within-tract topological organisation of fibres. Based on MRI tractography, Van Weeden proposed a sheet-like axonal organisation between tracts, with frequent right angle crossings (*4*), an interpretation that has been debated (*5*). Indeed, the limited spatial resolution afforded by diffusion MRI calls into question the modelling accuracy of sub-voxel fibre crossings and parallel fibres (*6*). Subsequently, Schilling et al. explored a potential resolution limit of crossing fibres by mapping the distribution of fibre orientations from histological images using the structure tensor model (*7*). They found that even at the scale of isotropic 32 μm, voxels still contain many crossing fibres. Hence, imaging modalities with still higher resolutions would be necessary to reveal the fine structure of axonal bundles. Notably, despite the limited image resolution of diffusion MRI, the water diffusion process itself can reveal geometrical features of structures at the micrometre scale such as axons and cell bodies, although such features compound at the voxel level(*8*). As such, complementary imaging techniques that directly image the axonal organisation could enhance the value of diffusion MRI.

MicroCT from lab sources or large-scale synchrotron facilities has been demonstrated as useful for validation of low-resolution MRI in small samples. Combining structure tensor analysis and streamline tractography applied to the microCT, Trinkel et al. demonstrated virtual mapping of the murine brain connectome of major pathways in comparison to tractography from diffusion MRI (*9*). In their work, they did not provide insights into the organisation of interfacing fasciculus bundles and were not able to resolve finer structures such as axons when using the resolution of MRI due to limited resolution.

X-ray holographic nanotomography (XNH) is another complementary imaging technique that enables nanoscopic image resolutions of intact axonal white matter in 3D using phase-contrast synchrotron imaging. By stacking image XNH volumes, Andersson et al. obtained an anisotropic field-of-view (FOV) of 600 micrometres, which is of comparable scale to a typical MRI voxel (*10*). Through segmentation of the larger diameter axons, they characterised the microdispersion of their trajectories using a measure of tortuosity, thereby revealing that the cross-sectional morphological changes along individual axons are imposed by structures in the local environment, i.e., cells, vacuoles, and blood vessels (*10*). Such 3D characteristics have provided new insights that improved microstructure MRI diffusion models (*11*, *12*). However, the Andersson study provided no analysis of the organisational features at the scale of axon fasciculus level due to the technical difficulty of segmenting full volumes. We

thus see a need for a sufficiently high-resolution imaging modality with a larger field-of-view (FOV) for exploring and quantifying axon fasciculus organisation (especially their interfaces) in simple and complex white matter regions. In this regard, Mortazavi et al., combined a neuronal tracer with structure tensor analysis applied to histological images to show that labelled axons of the major white matter pathways in the *centrum semiovale* cross each other in a grid-pattern (*13*). Moreover, Zhou et al. combined two different fluorescence neuronal tracers to show vertical stacking of parallel interhemispheric projections in the corpus callosum of mice (*14*). However, such approaches capture only a small number of labelled axons.

Recent advances in synchrotron imaging introduced hierarchical phase-contrast CT of the intact human brain, with selection of different FOVs and image resolution (down to 2.5 µm) within a single imaging session (*15*). Ideally, sub-micrometre imaging techniques are needed to be comparable to the microstructural features that diffusion MRI is sensitive to.

In this work, we applied a multimodal imaging approach, aiming to bridge the gap between diffusion MRI and the scale of the axonal fasciculi, aiming to reveal the 3D white matter organisation across different anatomical length scales throughout intact monkey and mouse brains, and in a murine demyelination model. We study two white matter regions of differing organisational complexity: The relatively simple and homogenous corpus callosum (CC), and secondly a complex crossing fibre region in the *centrum semiovale*. We use the term “anatomical length scales” throughout to designate anatomical features of different magnitudes – axons, bundles of axons (fasciculi), and tracts – that may have differing scales between mouse and monkey brains. To perform this multi-scale investigation, we apply a multi-modal imaging approach combining conventional diffusion MRI with sub-micron x-ray synchrotron phase-contrast tomography at two different synchrotron facilities: the Deutsches Elektronen-Synchrotron (DESY), beamline P10; and the European Synchrotron (ESRF), beamline ID16A. After diffusion MRI, we imaged volumes of interest at DESY (550 nm voxel size) and then at ESRF (75-100 nm voxel sizes). Each step produced images with increasing resolution, but in incrementally smaller FOVs. From the diffusion MRI data, we estimated tissue anisotropy using e.g. the diffusion tensor model (*16*) micro-tensor model (*17*), and modelled the fibre orientation distribution (FOD) using the multi-fibre constrained spherical deconvolution (CSD) model (*18*). In the x-ray synchrotron data, we applied a scale-space structure tensor analysis, which allowed quantification of tissue anisotropy. Here, we performed tractography on the main (or dominant) direction obtained from the structure tensor, and modelled axonal fasciculi based on the clustering of the tractography streamlines, with quantification of their deviations from linearity, i.e., tortuosity. By these means, we demonstrated a new organisational principle of white matter that persists across anatomical length scales and species, which governs the arrangement of axons and axonal fasciculi into sheet-like laminar structures. We found that these laminae have differing inclination angles with respect to each other, depending on their presence within parallel or crossing major pathways. Finally, we examined how demyelination in the murine model affected the diffusion MRI and structure tensor metrics.

2. RESULTS

2.1. Multi-scale, multi-modal imaging data in the monkey CC

We first acquired an ex vivo diffusion MRI image of the whole monkey brain, which was reconstructed with isotropic 0.5 x 0.5 x 0.5 mm^3 voxel sizes (Fig. 1A) (see methods section for details). We then obtained a thin needle biopsy sample of 1 mm diameter from the mid-body of the corpus callosum (CC) (Fig. 1B), which we imaged twice with phase contrast tomography; at DESY with 550 nm voxel size, providing fascicular resolution, and at ESRF with 75 nm voxel size, providing axonal resolution. At ESRF, we stacked four consecutive image volumes to create a large effective FOV (Fig. 1C). The relative sizes of an MRI voxel and the various synchrotron volumes are shown in Figure 1D. The dark image intensities in the synchrotron x-ray images (Fig. 1B, C) are due to osmium staining of the myelin.

As seen in the image acquired at DESY in Figure 1B, the staining only penetrated the outer rim of the biopsy sample. At this image resolution, resolvable structures include the largest axons (with diameters roughly >2.5 µm), blood vessels, clusters of cell bodies, and vacuoles. Cell bodies and vacuoles appear bright in contrast to their outlining myelinated axons, which appeared to be oriented mainly in the left-right (L-R) axis, as expected for a CC sample.

The high-resolution ESRF data has a field-of-view (FOV) of 0.21 x 0.21 x 0.21 mm. Fig. 1B depicts the placement of the FOV in the osmium-stained rim of the CC sample. The four stacked scans provide an extended FOV of 0.21 x 0.21 x 0.78 mm to match better that of the DESY volume and an MRI voxel (Fig. 1C). In this data, it is possible to observe and quantify fine microstructural details, i.e., axon morphology, myelin thickness, nodes of Ranvier, clusters of cell bodies, vacuoles, and blood vessels (for a detailed description see (*10*)).

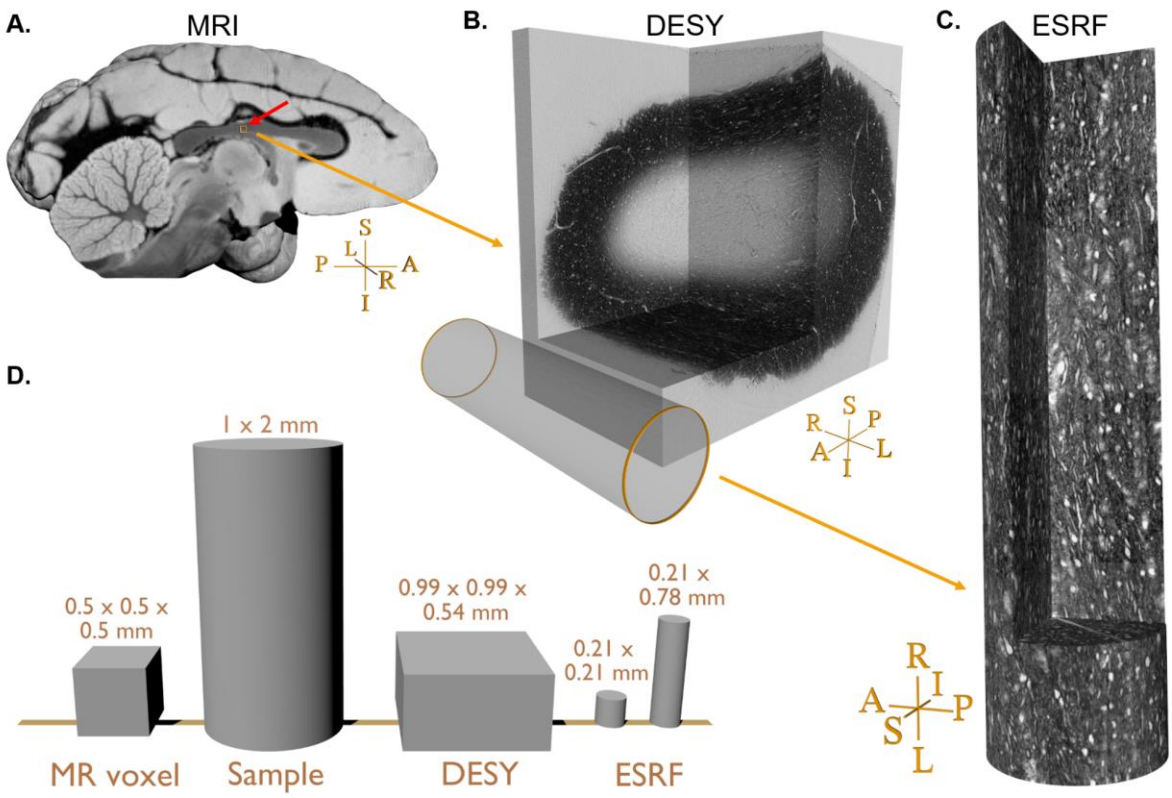

Figure 1: Sample comparison. A) Rendering of the vervet monkey brain structural MRI close to the mid-sagittal plane. **B)** Large field-of-view (FOV) scanning of the biopsy, DESY. The small orange box near the red arrow in A) indicates the location and size of the FOV within the MRI data. **C)** The stack of 4 small FOVs scans obtained at ESRF. The cylinder in B) indicates the relative size of the FOV within the DESY scan. **D)** Relative size comparison of one MRI voxel, the biopsy sample prior to staining and fixation, and various synchrotron FOVs. For cylindrical FOVs, the first number indicates the diameter, and the second number is the height. Sample orientations are related to the whole brain in A): R: Right, L: Left, I: Inferior, S: superior, A: Anterior, P: posterior.

2.2. Corpus Callosum: A "straight fibre" region in the monkey brain

The CC, the largest white matter tract in the brain, has high tissue anisotropy, being dominated by densely packed axon fasciculi that all run in the right-left direction between the two hemispheres (*10*). From the diffusion MRI, the directional colour-coding of the three eigenvectors from the diffusion-tensor model suggests that the axonal directions are locally consistent and symmetric around the midsagittal plane (Fig. 2A). The MRI voxel corresponding to the location of the synchrotron samples is located in the mid-body, approximately 2 mm lateral to the midsagittal plane (the white box in Fig. 2A). In this voxel, the estimated orientations of the diffusion tensor and CSD models (Figs. 2B and 2C) both have a main R-L component (red) with a strong I-S inclination (blue), and very little response in the A-P direction (green). The multi-fibre (CSD) model shows a single fibre peak, with a relatively narrow and isotropic spread of the fibre orientation distribution (FOD) when mapped onto a spherical polar histogram (Fig. 2B). This is consistent with a homogeneous microstructural environment dominated by densely packed parallel axons. Indeed, the diffusion tensor model predicted a high fractional anisotropy (FA) value of 0.861 (*19*) and even higher FA anisotropy in the micro-tensor domain of 0.997, i.e., the micro (μ)FA (*20*, *21*).

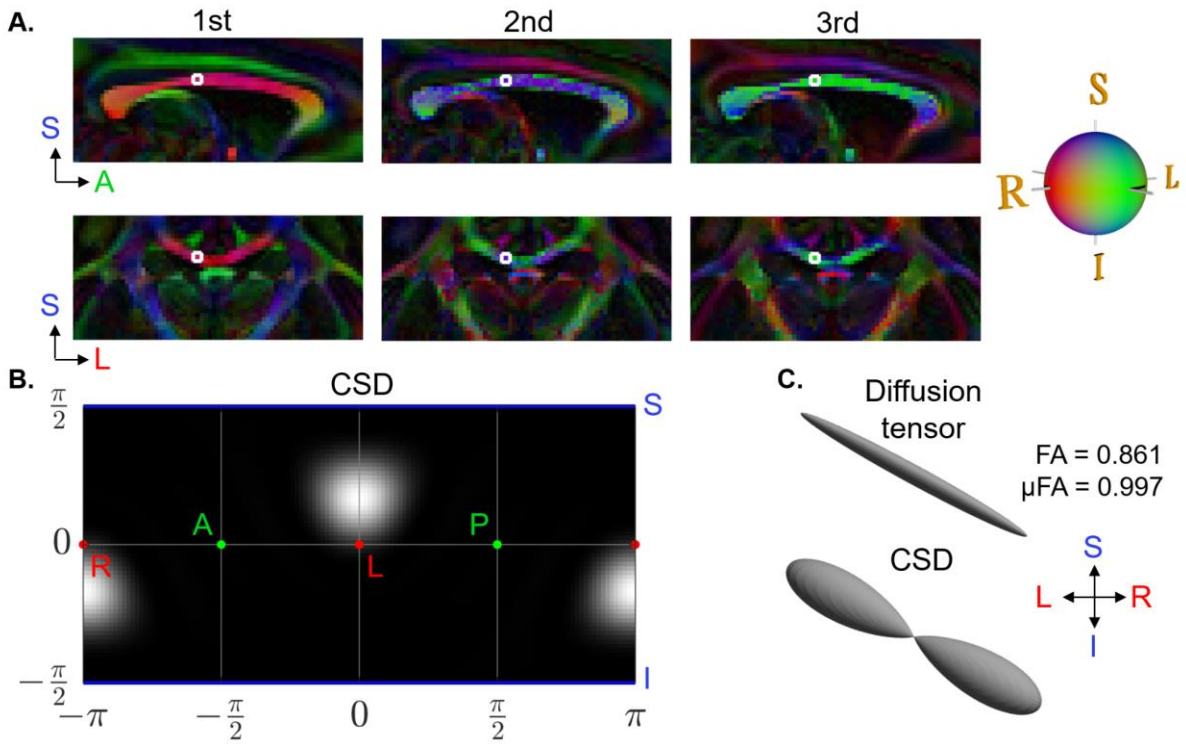

Figure 2: dMRI-based orientations and tensor shapes. A) The diffusion tensor model showing principal directions in a sagittal slice of the monkey corpus callosum (CC). The voxel corresponding to the biopsy sampling location (the synchrotron FOVs) is outlined in a white box. **B)** The fibre orientation distribution (FOD) of the CSD model in the selected diffusion MRI voxel is represented as a spherical polar histogram. **C)** The corresponding glyph representations of the diffusion tensor and CSD.

Our analysis of the high-resolution DESY data of the CC sample is shown in Figure 3 (A, C, and E). The structure tensor was estimated based on a single set of scale-space parameters, corresponding to an integration patch size of 12 microns (see methods for further details), which is sufficient to detect all tissue-relevant orientation features. Interestingly, the structure tensor directional colour map in Fig. 3A (yellow-green bands) indicates laminae of axon fasciculi with a thickness of up to 40-45 μm projecting throughout the whole cross-section of the CC sample. These laminae have inclination angles up to ~35 degrees from the right-left (R-L) axis. Figure 3C shows a subset of the structure tensors visualised as 3D glyphs overlaid onto an image from the synchrotron volume. At this image resolution, the structure tensor directions follow either blood vessels or axonal structures.

Upon mapping the structure tensor principal directions within the image volume onto a spherical polar histogram (Fig. 3E), we observe a FOD having a single fibre peak. The I-S inclination angle is smaller than that of CSD from diffusion MRI (Figs. 2B, C). Figure 3F illustrates the elongated shape of the structure tensor FOD towards the R-L axis, reflecting a degree of fibre dispersion originating mainly from the axonal laminar organisation visible in Fig. 3A (black arrows).

From the ultra-high image resolution ESRF data shown in Figure 3 (B, D), we estimated the structure tensor at different scales, corresponding to patch sizes ranging from 9.2 - 2 µm. This allowed for the detection of tissue anisotropy on different anatomical length scales, i.e., corresponding to blood vessels, large axons, and small axons. The structure tensor directional colouring (Fig. 3B) does not capture the layered laminar organisation seen in the DESY data. This may be explained by the smaller FOV (210 µm) not covering a cross-sectional volume in which the laminar organisation appears. However, smaller laminae with a thickness of up to 20-25 µm are discernible in Figure 3A.

The direction vectors of the structure tensor analysis from all four stacked ESRF volumes are converted to spherical polar coordinates in Figure 3H. The histogram resembles that representing the DESY data (Fig. 3E), except that the main direction of the ESRF data has a lower inclination angle in the I-S axis. An exact co-registration of the two synchrotron volumes was not feasible, and some discrepancies between the FODs are to be expected.

In Figure 3G, we present the calculated distribution of FA values of the structure tensor for the four stacked ESRF volumes, intended to match approximately a single MRI voxel. The mean FA value of the ESRF data was higher than in the DESY data (0.67 ± 0.05 versus 0.54 ± 0.09, respectively) and the ESRF data distribution was narrower than in the DESY data, i.e., (ESRF median/Inter quartile range (IQR): 0.68/0.06, DESY median/IQR: 0.55/0.12). The high anisotropy at the micrometre-scale image resolutions is in accord with the FA value of 0.861 and µFA of 0.997 in the dMRI voxel, as shown in Fig. 2C. Although the two synchrotron volumes originated from the same biopsy, the FA distributions are not identical. Visual inspection reveals that smaller axons and cell bodies are hardly distinguishable in the DESY data (Fig. 3A) but are clearly evident in the higher resolution ESRF data (Fig. 3B).

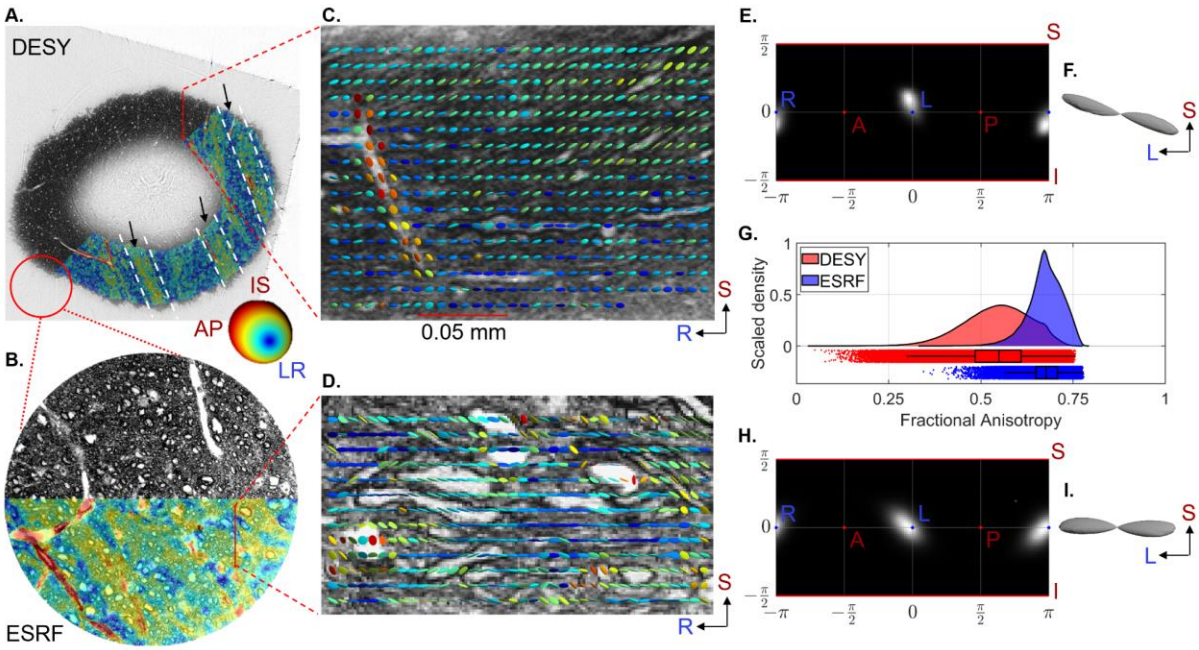

Figure 3: Structure tensor shape for corpus callosum (CC) sample. A-B) Sagittal slices from respectively the DESY and ESRF CC biopsy sample with structure tensor main direction colour coding (in accordance with the colour sphere). The white markings and black arrows illustrate bands where axons are oriented at an angle compared to their surroundings, indicating a laminar organisation. The red circle on (A) shows the scale difference between the DESY and ESRF data. The position of the sample within the CC is marked on the MR image in Figures 1A and 2A. **C-D)** Selected coronal slice overlaid with a regularly spaced subset of structure tensor glyphs, coloured according to their predominant direction. **E- F)** Spherical polar histograms of the DESY structure tensor main directions (FOD) and the corresponding glyph. **G)** Kernel density estimates of structure tensor FA values. **H-I)** Spherical histogram of the ESRF structure tensor main directions (FOD) and the corresponding glyph. NB: We exclude contributions from the voxel of blood vessels in FA histograms and FODs.

2.3. Deep white matter: A “complex tissue” region in the monkey brain

We next investigated the axonal organisation in the *centrum semiovale* in deep white matter. The region contains up to three major pathways that are potentially crossing, i.e., the corticospinal tract, the CC, and the superior-longitudinal fasciculus (*22*). We imaged this complex tissue sample with dMRI and ultra-high resolution synchrotron imaging at the ESRF, and then applied a structure tensor analysis using the same range of scale-space parameters as for the CC sample, i.e., focusing on contrasted tissue features of size in the range of 9.2 - 2 µm.

Figure 4A shows the CSD FOD multi-fibre reconstructions from dMRI of a region encompassing the sample puncture. Due to the image resolution of dMRI and the known regional complexity of fibre organisation, most voxels contained more than one fibre peak, which indicates the expected presence of crossing fibres. Fig. 4A (white circle) highlights the dMRI voxel best matching the FOD in the synchrotron imaging volume; it contains three fibre components, as shown by the spherical polar histogram (Fig. 4B) and the corresponding glyph (Fig. 4C). The two largest peaks (“parallel fibres”) are S-I directed (blue) and the smaller peaks points mostly in the R-L direction (red).

The synchrotron data from *centrum semiovale* shows axons tending to organise in a laminar-like style similar to that in the CC. The laminar thickness ranges from as little as 5-10 µm to as much as 35-40 µm. Some laminae are predominantly populated by axons of small diameter, too small to segment individually at this image resolution. Other laminae include a mixture of populations of different diameters. Some axons intermingle with a neighbouring lamina (Figure 4E). The laminar finding holds across the four stacked sub-volumes.

The structure tensor FOD within the ESRF volume (Fig. 4F, G) has one strong S-I and one weak R-L directed peak, much as seen in the diffusion MRI (Fig. 4B, C). The largest discrepancy between the FODs of the two modalities lies in the presence of a secondary S-I directed peak in the dMRI data (Fig. 4B, C).

Finally, the estimated FA of the diffusion tensor within the single dMRI voxel (0.350) was much lower than that in the micro-tensor (0.993). The low FA value of the diffusion tensor model is expected as it cannot handle the complex fibre crossings (*20*, *21*), whereas the micro-tensor is modelled to be independent of the axonal organisation.

The structure tensor FA histogram from the ESRF data (Figure 4H) had a median value of 0.66 and IQR 0.07. Interestingly, the structure tensor FA histograms of the “complex region” and the “straight fibre” regions (Figure 3G vs. 4H, respectively) are almost identical, suggesting that the given scale-space structure tensor is independent of fibre organisation, similar to the diffusion micro-tensor model (µFA).

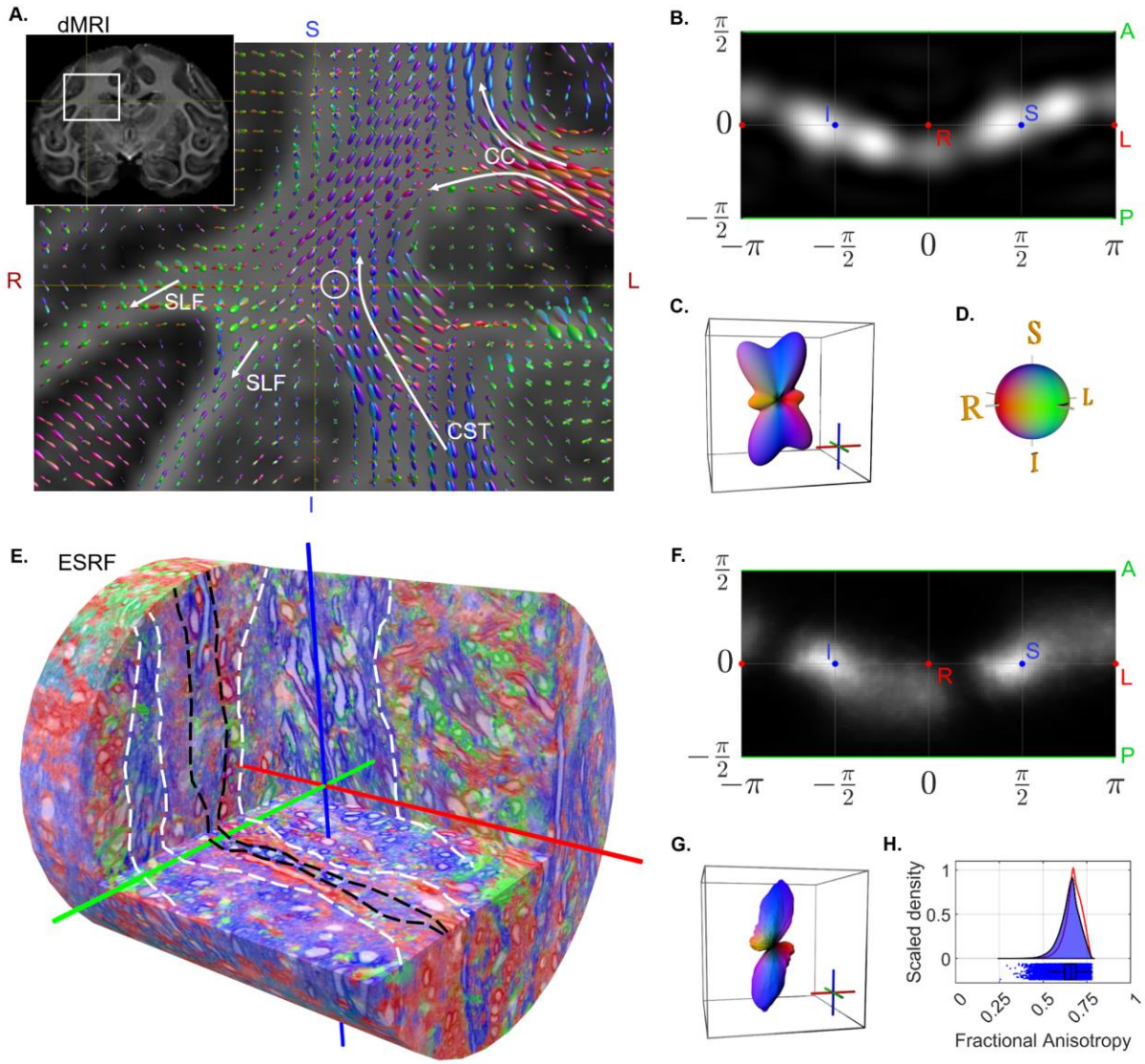

Figure 4: Results in complex monkey deep white matter (WM) region. A) Anatomy and CSD glyphs seen in the volume surrounding the local neighbourhood of the sampled biopsy location (white circle). **B and C)** Results in the matching MRI voxel, showing FOD (CSD) and the corresponding glyph. **D)** The directional colour map used throughout the figure. **E)** Example of rendering from an ESRF volume with colouring corresponding to the structure tensor main direction. Marking with dashed lines indicates clear fasciculi. **F and G)** Structure tensor directional statistics from the stacked FOV, showing the structure tensor FOD and corresponding glyph. **H)** Structure tensor shape statistics from the stacked FOV, showing the kernel density estimate of FA values. The red curve is a copy of the FA distribution from the ESRF CC region (Fig. 3G).

2.4. Axon fasciculi trajectories in straight and complex tissue samples

To explore the macroscopic axonal organisation and trajectory variations of fasciculi at the MRI sub-voxel level, we applied streamline tractography (*23*) to the main direction of the structure tensor analysis of the synchrotron data. We manually drew seeding regions to delineate where we expected axons to project towards within the sampled volume (see Methods section). To ease visualisation and quantification, we used QuickBundle clustering (*24*) to collect neighbouring streamlines with similar trajectories into a centroid streamline that roughly represents the trajectory of a fasciculus. For simplicity, we designate such a centroid streamline as streamline.

Tractography in the DESY corpus callosum data revealed evenly distributed streamlines throughout the sample (Figure 5A). The streamlines all follow a primary L-R direction, and a large portion of the trajectories follow a small S-I bending (coloured purple), which is in good agreement with the local FODs both from structure tensor and CSD dMRI data (Figure 2 vs. 3). Depicting the portion of streamlines without a strong S-I direction component with a separate colour (Fig. 5A, cyan streamlines) conveys the laminar organisation also observed in the structure tensor analysis (Fig. 3A). The inclination angle between the trajectory of the two streamline laminae is about 35 degrees.

For the ESRF data, the streamlines typically represent the trajectory of a small number of axons, and even in some cases of single large diameter axons. As such, the streamlines in ESRF data (Fig. 5C) better reflect detailed axonal trajectory variations as compared to the DESY data. For example, streamlines in the CC show non-straight trajectories that circumvent neighbourhood obstacles such as clusters of cell bodies, other axons, and blood vessels (orange structure). Interestingly, we observed several small axons crossing the FOV orthogonal to the otherwise dominant R-L organisation. This phenomenon was particularly evident along the blood vessels, as illustrated in Figure 5C (purple streamlines).

As expected, streamlines in the ESRF *centrum semiovale* data, followed the main direction of the laminae identified in the structure tensor directional map seen in Fig. 4F. Figure 5D shows the trajectory of streamlines coloured according to the local direction, i.e., R-L (red), A-P (green) and S-I (blue). Independent of the main direction, we observe streamlines skirting around local obstacles and other axons, resulting in more complex and less straight trajectories than in the CC region.

To quantify the shape of fasciculi trajectories through the image volume, we characterised each streamline with two scalar values: (1) the streamline tortuosity index, which is a unitless score in [1, ∞] describing the deviation from linearity, and (2) the calculated maximum physical deviation from a straight line of each streamline, which depicts the maximal axonal “amplitude” or dispersion. Both scalar metrics are independent of the general fasciculus orientation, but reflect micro-dispersion that can impact dMRI estimations (*10*, *25*). We estimated the distributions of tortuosity and maximum deviation for all streamlines in both the DESY and ESRF samples (Fig. 5B).

In the CC, the mean tortuosity index of the distribution was identical in the DESY (1.03 ± 0.01) and ESRF sample (1.03 ± 0.04). A tortuosity index close to unity is equivalent to highly straight fibres, consistent with the visual inspection of the streamlines (Figure 5, A and C), and likewise with our expectation for the CC. In contrast, the mean observed maximum deviation within the samples differed distinctly between DESY (22.6 ± 10.7 μm) and ESRF (5.1 ± 3.3 μm). In ESRF data, the small FOV limits the analysis to capture only microscopic effects.

Therefore, the maximum deviation is driven by the interaction of the fasciculus with neighbourhood obstacles, i.e., micro-dispersion. We observed maximum deviations as high as 12 μm, which were due to obstacles like blood vessels, thus in good agreement with observations reported in (*10*). In DESY data, deviations were as high as 40 μm, which we attribute to more macroscopic effects such as the bending of pathways, as observed in Figure 5A. We suppose that this may arise from the U-shaped macroscopic trajectories of CC fibres towards the cortex.

In the ESRF *centrum semiovale* sample, the mean tortuosity index was significantly higher and more variable (1.09 ± 0.12 μm) than in the CC. This agrees with the more complex crossing fibre trajectories observed in Fig. 5D. Interestingly, the distribution of maximum deviations had a peak around 5.3 μm and a mean of 10.7 ± 7.5 μm. While it is an increase compared to the CC, the magnitude of streamline dispersion is on a comparable scale.

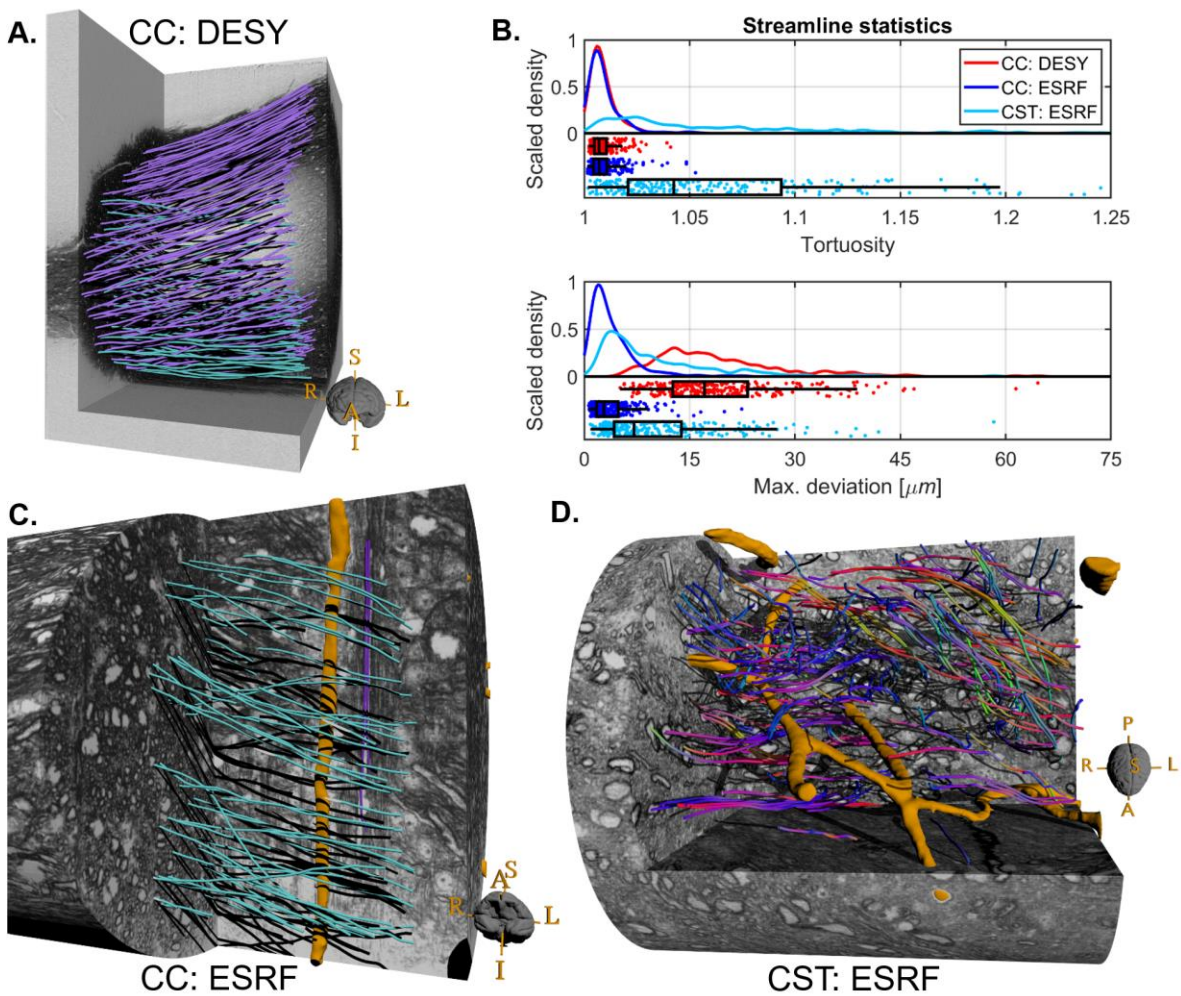

Figure 5: Structure tensor-based tractography for the monkey samples. A) Streamlines in the CC sample from DESY. Purple streamlines have a strong upwards directional component, unlike the cyan streamlines (assuming that streamlines travel from right to left). **B)** The statistics of streamlines quantification using tortuosity index and maximum deviation. **C)** A selection of streamlines in the CC within a single ESRF scan. Cyan streamlines have R-L as the strongest directional component, whereas purple streamlines do not. The orange structure is a segmented blood vessel. **D)** Streamlines in the complex *centrum semiovale* region (CST) within a single ESRF scan. Streamlines are coloured according to their local main direction. Orange structures represent segmented blood vessels.

2.5. Multi-scale, multi-modal imaging data in healthy and demyelination mouse brains

Finally, we explored the organisation of fasciculi in the healthy mouse brain and in a murine model of focal demyelination induced by cuprizone (CPZ) treatment for five weeks. The experimental setup for DESY and ESRF is similar to that described above for the monkey, except that we did not undertake dMRI and synchrotron imaging of the same brains, and only collected MRI for healthy mouse brains.

The dMRI is a whole-brain FOV, whereas the FOVs of DESY and ESRF are similar to those for the monkey (see Table 1). The image voxels of dMRI, DESY and ESRF have isotropic side lengths of 125 µm, 550 nm and 75-100 nm respectively. Although the mouse brain image resolution of the DESY and ESRF data is similar to that acquired on the monkey, the white matter structures in the mouse brain are considerably smaller in proportion, and the resolvable anatomical length scale differs. In the mouse, the FOV of the DESY data included both the splenium region of corpus callosum and parts of the neighbouring Cingulum bundle (Fig. 6A). Further, in the ESRF data, the image resolution did not suffice to outline the diameters of even the largest axons (Fig. 6B), in contrast to the monkey CC. However, blood vessels and glial cells are outlined as the stained myelinated axons skirt around them. Unlike in the monkey samples, we did not observe vacuoles in the mouse samples.

DESY and ESRF data both revealed demyelinated regions in the CC of the cuprizone-treated mouse. The lesion area is demarcated by an intensity gradient increasing from dark (intact myelination) toward a brighter signal (demyelination) (Fig. 6C, D). In the demyelinated area, the ESRF data revealed a higher density of cell bodies and small accumulations of heavily stained material. Cellular structures were manually segmented in a small representative region to reveal their 3D shapes (Fig. 6E).

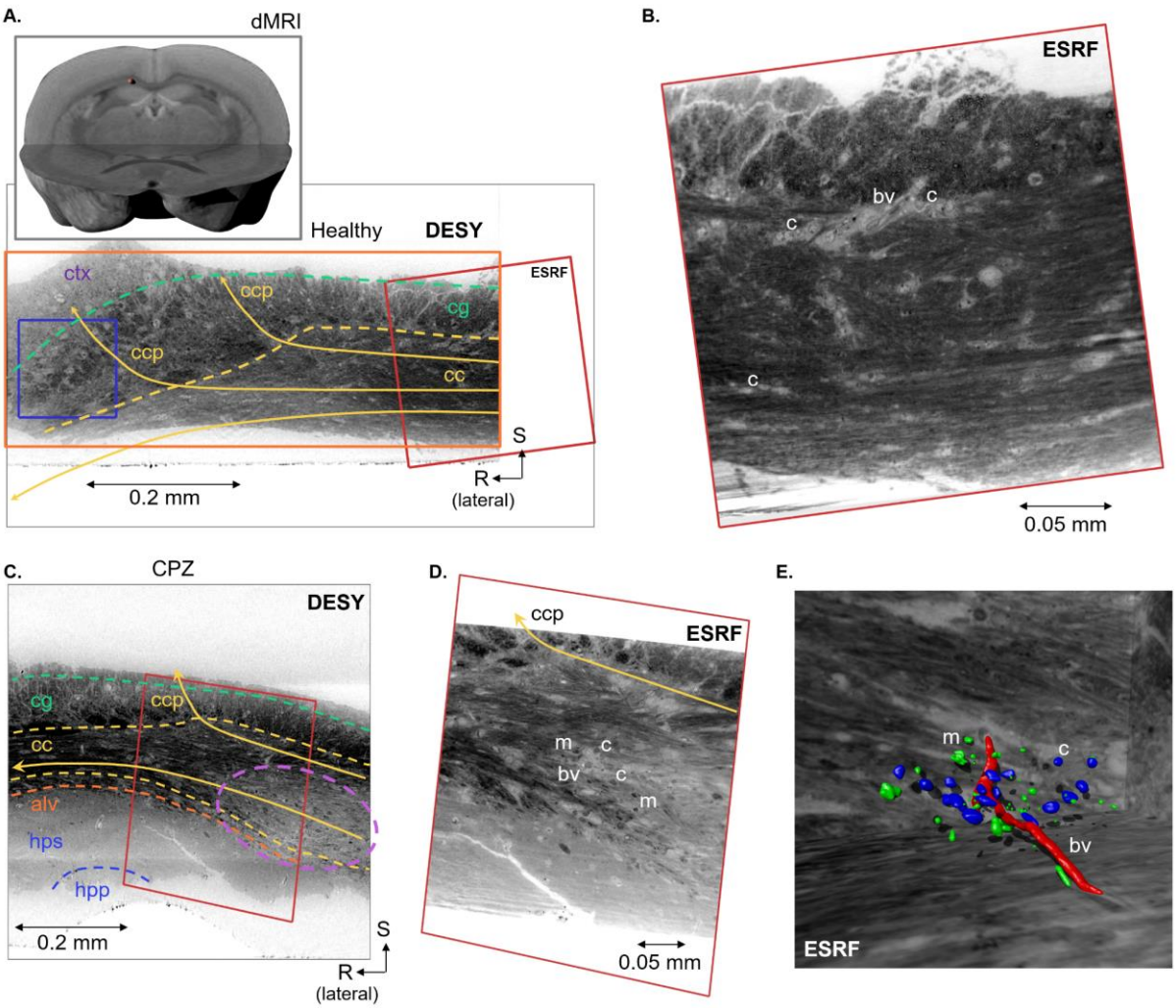

Figure 6: Overview of the mouse datasets. A) Location of the sample within the mouse brain and a coronal slice from the DESY dataset, with indications of anatomic regions: cc = corpus callosum, cg = cingulum, ctx = cortex, and ccp = cortical projections. The blue box indicates the size of a DWI voxel. **B)** The co-registered slice from the ESRF volume (position indicated by the red frame). Labels indicating blood vessels (bv) and cells (c). **C)** Coronal slice from the DESY dataset of a CPZ-treated mouse, with indication of anatomic regions: cc = corpus callosum, cg = cingulum, alv = alveus, hps = hippocampal striatum, hpp = hippocampal pyramidal layer, ccp = cortical projections. The dashed purple line shows a demyelinated region of the CC. **D)** The co-registered slice from the ESRF volume (indicated by the red frame). Labels indicate blood vessels (bv), cells (c), and myelin 'debris'/macrophages (m). **E)** 3D rendering of the corresponding region with a local segmentation of structures (blood vessels in red, cells in blue, and 'myelin debris' in green).

Preservation of the organisation of major pathways in healthy and demyelination mouse brains

In dMRI of the healthy mouse brain, the colour-coded diffusion tensor directions of the first (major) principal direction have the same R-L direction (red) as seen in the monkey (Fig. 7A vs. 2A). However, Figure 7A shows a shift of the second and third principal directions in the mouse CC, as compared to the monkey.

In the healthy and demyelination mouse brains, we use only a single scale-space level for the structure tensor patch size (see method section) both in the DESY and ESRF data sets. The integration patch sizes correspond to 18.7 µm for the DESY and 9.4 µm for the ESRF samples (see Table 2).

In the DESY data from healthy mice, the directional colour coding of the structure tensor was in accord with the diffusion tensor MRI (Figure 7A vs. B). We found sporadic directional deviations in the coronal view, represented as local regions with different directional colours in Fig. 7B, which indicate local crossing axon fasciculi and/or blood vessels. Nevertheless, we see no strong indication within the mouse CC of the axonal laminar organisation observed in the monkey (Fig. 3A).

The two major pathways, the CC and cingulum bundles, appear in the mouse as two sharply separated structures crossing almost orthogonally on a grid. This clearly reflects in the 3D glyphs of the structure tensor FOD for the ESRF and DESY data sets (Fig. 7E). In the structure tensor FOD, the variance around the CC peak exceeds that in the cingulum bundle.

The structure tensor FA histograms of the mouse CC and cingulum bundle, both are shifted toward lower values in the DESY data as compared to the ESRF data (Fig. 7G). The two histograms overlap in the DESY data, whereas the ESRF data shows a shift towards higher FA values in the cingulum as compared to CC, indicating a dependency of the estimated FA on image resolution relative to the size of structures. From the ESRF data we were able to roughly segment cell clusters and blood vessels. Since the volume consists of about 13.5% cells/blood vessels in the cingulum bundle, versus only 8.5% in CC, the higher density of extra-axonal structures may factor into the differences in estimated FA values.

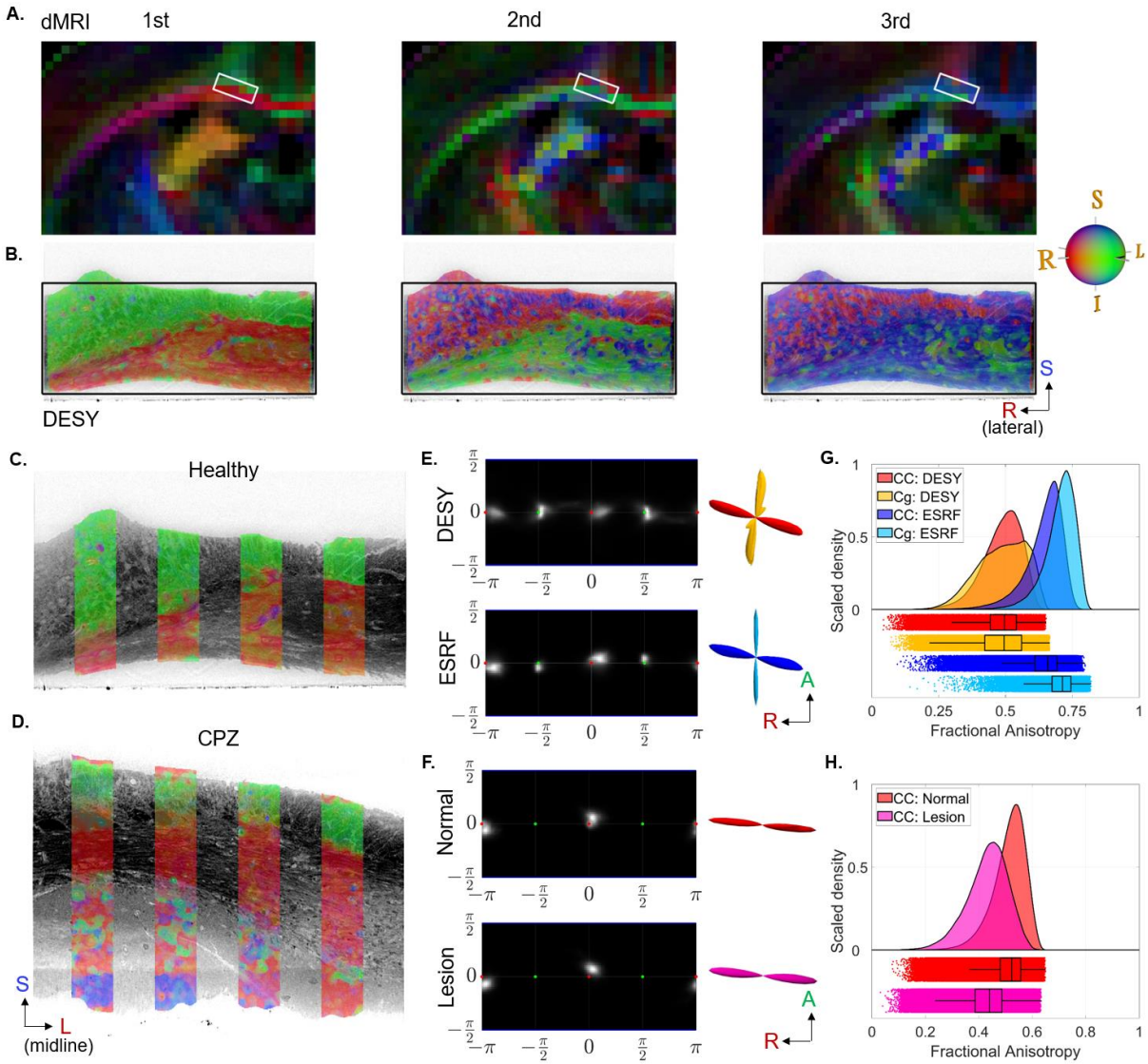

Figure 7: Mouse diffusion tensor and structure tensor results: A) and B): The directional components of the diffusion tensor and the structure tensor in a coronal slice from a healthy mouse brain. The white frame in (A) indicates the approximate size and location of the DESY FOV, i.e., the black frame in (B). **C) and D)** The main structure tensor direction from the DESY data overlaid on a slice from a healthy mouse brain (C) and a CPZ-treated mouse (D). **E)** Structure tensor FODs from a healthy mouse along with corresponding glyphs. The glyph colouring indicates whether the FOD contribution is from the CC (red/blue) or cingulum (yellow/cyan). **F)** structure tensor FODs from the CPZ-treated mouse CC (DESY), split into contributions from a normal appearing region and a demyelinated area. **G) and H)** structure tensor FA distributions from various regions of healthy and lesioned mouse samples.

In the CPZ-treated mouse brain, the directional colour-coded structure tensors in the DESY data match that in the healthy mouse, even in the demyelination region, which shows reduced image contrast (Fig. 7C vs. D). The fact that there even is directional contrast in the demyelinated region, depicts the advantage of phase-contrast imaging, where the obtained contrast is not solely dependent on absorption. Note that the demyelination region is confined to axons within the CC, with sparing of the cingulum bundle. The lower image contrast (lack of strong edges) in the demyelinated region contributes to the blurrier tensor shapes and lower FA values as compared to the normal-appearing white matter (mean FA: 0.44 vs. 0.52), as shown in Fig. 7H.

Axon fasciculi trajectories in healthy and demyelination mouse brains

For better comparisons, we registered the ESRF data of mouse CC onto the DESY data. In healthy and cuprizone-lesioned mice, Figure 8A, B shows that the CC and cingulum bundle are both mappable using streamlines. Irrespective of image resolution, the cingulum bundle did have a lower tortuosity and maximal deviation than the CC (Fig. 8C, E), which could be due to differences in densities of extra-axonal structures. This is suggested by the streamlines projecting through the demyelinated region (Fig. 8B), which contains more cells (Fig. 6D, E). Indeed, both indices broadened with lower image resolution in combination with a larger FOV that covers macroscopic shape changes. An example is the bending of corpus callosum detected by the longer streamlines.

Interestingly, both in healthy and demyelination samples, some streamlines from the CC corpus deviate to project into the cortex, as illustrated in Fig. 6 and Fig. 8A, B (pink extensions of streamlines). Those that project into the cortex also tend to originate from a more superiorly placed seed point. As such, the streamlines present a vertically layered organisation within the CC.

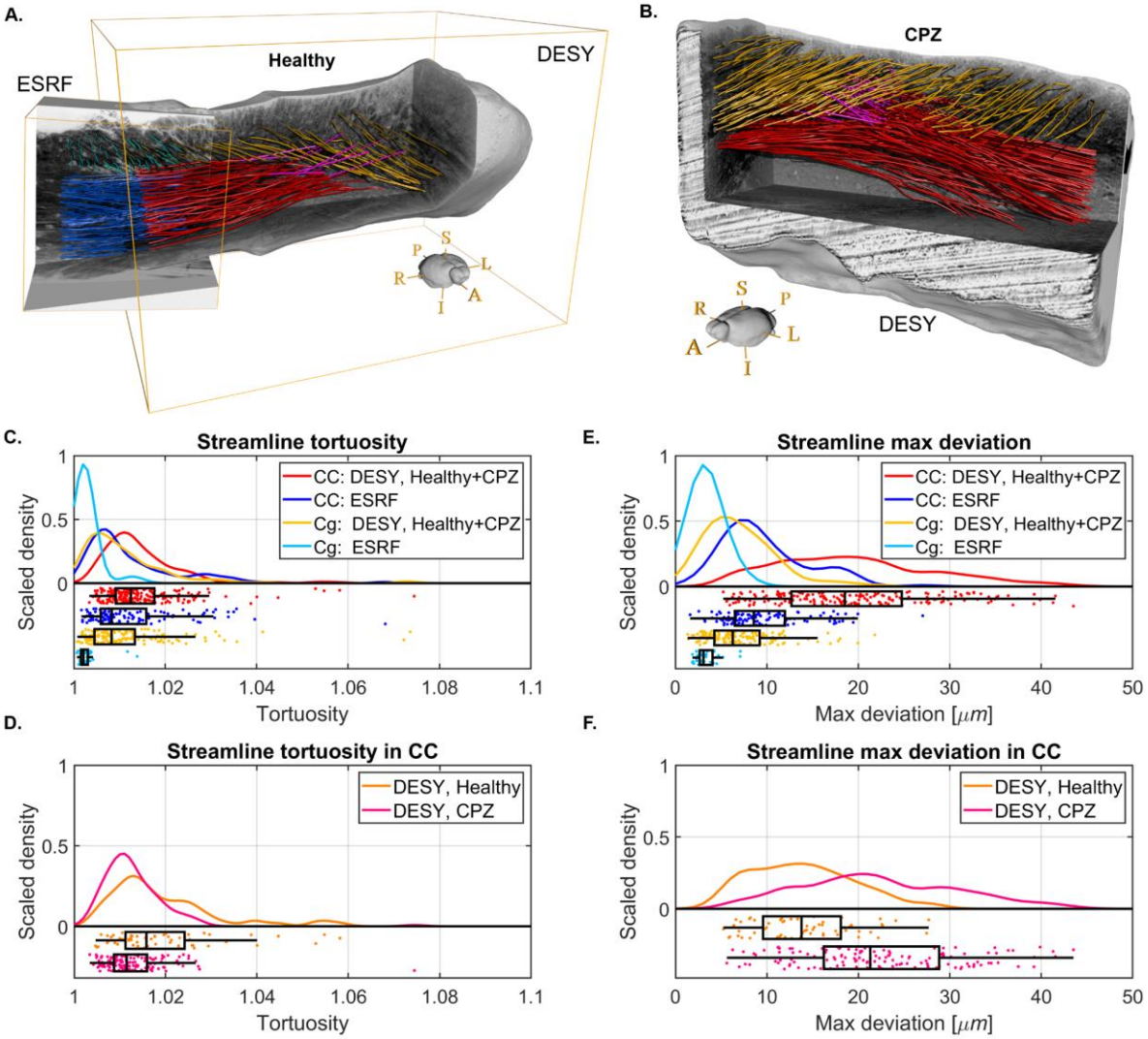

Figure 8: Mouse tractography results. A) Tractography visualisation from a healthy mouse brain sample. Red and Blue: Streamlines in CC. Yellow and Cyan: Streamlines in cingulum. Pink streamlines are extrapolations of CC streamlines that represent plausible cortical projections through the cingulum. **B)** Tractography visualisation from DESY data of a CPZ-treated mouse brain. **C) and E)** Tractography streamline centroid statistics from the healthy mouse brain synchrotron volumes. The curves are kernel density estimates of the tortuosity and maximum deviation, respectively. **D) and F)** Statistics for the streamlines in the corpus callosum of the DESY healthy and CPZ mouse brain samples.

3. DISCUSSION

By combining diffusion MRI and high-resolution phase-contrast synchrotron imaging, we quantified the 3D organisation of fibre pathways in white matter across a range of anatomical length scales. Importantly, our findings revealed common principles of fibre organisation in both monkeys and mice; small axonal fasciculi and major bundles formed sheet-like laminar structures, with relative angling that depended on the characteristics of the major pathway to which they belonged. By applying a scale-space structure tensor analysis and streamline tractography to the synchrotron datasets, we quantified the micro-dispersion of individual axons and fasciculi. Interestingly, the dispersion magnitude is indicative of fasciculi that skirt around obstacles in the white matter such as cells and blood vessels, and the results are largely independent of both white matter complexity (straight vs crossing fibre region) and pathology. Our dMRI and scale-space structure tensor analysis allowed us to compare and quantify tissue anisotropies and fibre orientations. We found that FODs were consistent across image resolutions and modalities, but only given that the FOV is the same. Estimates of microscopic FA were highly correlated across modalities. However, to achieve good specificity in the anatomical feature correlation the diffusion tensor and structure tensor models must be sensitive to the same anatomical length scale.

Laminar organisation across image resolutions and modalities

Our white matter samples from monkey and mouse brains were geometrically organised as stacked laminae across anatomical length scales extending from individual axons to axon fasciculi and the major bundles.

In the relatively lower image resolution DESY data with a larger FOV - on the scale of a dMRI voxel - revealed a columnar laminar organisation at the macroscopic level in the monkey CC, which was not visible in the higher resolution ESRF data for the same monkey brain tissue sample. As such, the higher image resolution in conjunction with lower FOV meant losing the clear detection of the larger scale laminar organisation seen in the DESY data.

Invasive tracer studies and histology in monkeys (*26*, *27*) and histology of humans (*28*) previously hinted at a columnar organisation in the ventral part of midsagittal CC. However, the earlier approaches failed to show the finer 3D columnar organisation of 10 µm thick laminae as revealed by the present structure tensor analysis of the synchrotron data. The occurrence of these thin layers with slightly different angles may be confirmed by visual inspection of polarised light imaging (PLI) data collected in a human brain coronal CC slice (in Fig. 6 of (*28*)). In a coronal view of the mid-sagittal region, PLI showed fibres arising from the right and left hemispheres reaching the midsagittal CC as a layered structure, based on its orientational colour coding. The greater slice thickness (in PLI 100 µm) in a coronal view may have resulted in a partial volume effect arising from the thinner non-parallel columnar laminar sheets that we observed in the sagittal view of our synchrotron data (Fig. 3A).

The imaging capabilities at synchrotron facilities are continuously improving. Faster acquisitions and better processing software is enabling large FOV scans through the stitching of individual sub-scans. The possibility to elucidate, for example, the 3D CC organisation of intact tissue on a scale amenable to PLI is approaching (*15*).

Structure tensor analysis of the present ESFR data in the complex fibre region clearly shows the crossing of three pathways composed of laminar sheets of fasciculi (Fig. 4E). Compared to the parallel within-tract axonal fascicles in the monkey CC, the boundaries

between fascicles in the complex fibre region are thin (10s of micrometres), and therefore likely to be less well defined when visualised as streamlines. However, we did not see such an intermingling of streamlines at the interface between the crossing of the larger well-defined tracts such as the CC and cingulum in the mouse brain (Fig. 7B-D).

The inclination angle between fasciculi

The structure tensor method performed very well in analysing the fasciculi without segmentation, through its detection of tracts and fasciculi based on their angular differences and highlighting of their sheet-like and laminar organisation. The observed tendencies regarding fasciculi organisation can be grouped into two: Within-VM pathways where inclination angles are low, and between-VM pathways where the angles are high.

Within major WM pathways, neighbouring axonal fasciculi appeared to follow the same principal direction but could have inclination angles up to the order of 35 degrees in both species.

Compared to the monkey, a laminar organisation was not obviously visible in the mouse CC from the structure tensor directions. However, the present streamline tractography is suggestive of a vertical layered organisation (Fig. 8A, B), which agrees with histological tracer mapping showing a stacked parallel organisation of callosal projections in mice (*14*). As such, we cannot rely solely on the structure tensor directions to fully describe axonal organisation, as the method does not contrast almost parallel fasciculi (inclination angles approaching 0-degree). Analysing the patterns in the tractography streamlines would be an interesting future direction for this purpose.

Interestingly, the default multi-fibre dMRI CSD model for the monkey CC showed only a single fibre direction with an isotropic FOD, indicating a coherent fibre bundle (Fig. 2C). This approach did not reveal any of the layering and organisation evident from structure tensor analysis of the synchrotron data (Fig. 3). Nevertheless, when investigating the directions of the diffusion tensor model we see signs that the diffusion signal is indeed sensitive to the complexity of fasciculi organisation; the principal direction agrees with the CSD and is locally consistent across the entire CC. However, the 2nd and 3rd eigenvectors are also informative, in that they behave symmetrically across the midline, and are locally consistent, although their order can shift at specific locations. This is likely an indication of the local organisation, similar to PLI-based observations (*28*). Additionally, Tax et al. have demonstrated the calculation of a sheet probability index from diffusion MRI data, which suggested the presence of sheet-like features in the CC and in a crossing fibre region (*29*), which is in line with our findings in the synchrotron data.

By further exploring the diffusion tensor modelling of the CC in the Human Connectome Data set (N=4, Fig. S1) we found an order of the 2nd and 3rd eigenvectors resembling that in the dMRI of the monkey. This observation supports the future exploration of the diffusion-weighted signal to reveal insights about axonal organisation. For the present, we have demonstrated axonal organisation only in select regions of the WM, but further research may establish more generalised rules governing fasciculi organisation in WM pathways, and potential species-related differences.

Between-WM pathways, the fasciculi cross with high inclination angles approaching 90 degrees. This is readily detectable in diffusion MRI multi-fibre CSD modelling (*30*) and in the structure tensor analysis. We observed this right angle crossing at the *centrum semiovale*, a complex fibre region with the crossing of three different pathways (Fig. 4). Using tracer

labelling of axonal projections, Mortazav et al. revealed grid-like right-angle crossing of axons in a similar region in the monkey brain (*13*). Tractography and micro-dissection findings of Wedeen et al. of the same region similarly showed grid-like crossing of laminar from different pathways (*4*).

Interestingly, we observed in the ESRF data a single axonal fasciculus composed of a few axons that crossed the main callosum bundle at an almost 90-degree angle running parallel to a blood vessel (Fig. 5C). Such phenomena may be overlooked in lower resolution data and have such a small contribution to the diffusion MRI signal as to be dismissed as noise/artefact. Without prior knowledge of their existence, such crossings are apt to be disregarded by modelling choices, such as orders of spherical harmonics, model regularisation, and number of fibre populations.

Our findings of laminar organisation and the distinction between high and low inclination angles seem to support a simple topological rule across anatomical length scales. This holds especially for the low inclination cases, which retain their laminar organisation with minimal intermingling in the neighbourhood, meaning that we expect that topological organisation should be kept over a distance. If so, the (inclination angle) information might serve to form rules for low-resolution diffusion MRI based tractography about how best to project through bottleneck regions, which is currently a source of false-positives trajectories (*6*).

Sources to the non-straight trajectories of axon fasciculi

Applying streamline tractography to the main fibre orientations in the structure tensor analysis enabled a geometric quantification of the non-linearity of axon fasciculi trajectories as a tortuosity metric (*31*). Surprisingly, we observed that the maximal amplitude of the axon fasciculi was comparable when measured in the crossing and straight fibre regions. This suggests that the geometrical variation in an axon fasciculus trajectory may hold similarly throughout the white matter.

We also detected differences in minor pathways: In the mouse brain ESRF data, axon fasciculi were straighter (i.e., having lower tortuosity) in the cingulum bundles than those in the corpus callosum. Similarly in monkey ESRF data, fasciculi were straighter in the CC than in the crossing fibre region.

For the monkey and mouse brain samples, the distributions of maximal deviation in the ESRF and DESY data showed main peaks around 5-7 µm. This range of maximal deviation aligns with the typical radius of the cell bodies. Indeed, axons and fasciculi have been observed to skirt around oligodendrocytes in the ESRF monkey data set (*10*). In addition, the maximal deviation is in accord with the size of a single axonal fasciculi (Fig. 5C) or blood vessels.

Even in the case of regional demyelination in the cuprizone-treated mice, we saw minor changes in tortuosity compared to normal axon fasciculi (Fig. 8D). We suppose that microglia and macrophages invading the site of demyelination are sufficiently similar size to oligodendrocytes that they have little net effect on the distribution of tortuosity. The measured max deviation was higher in the cuprizone-treated mouse (Fig. 8F), but given the magnitude of approx. 30 µm, this effect is more likely a description of the macroscopic bending of the CC, rather than a result of the demyelination. As our streamlines went through both demyelinated and normal appearing regions of the CC, we experienced a similar dilemma found in MRI-based tractography applied in humans. The streamlines are based on only the direction of the

tensor and are not guaranteed to be sensitive to local pathology. Additionally, demyelination is a dynamic process. We only sampled a single time point, and more must be included to explore if tractography-based analysis has the sensitivity to correlate with the temporal dimension of demyelination.

Diffusion MRI is sensitive to the micro-dispersion effects (*10*, *32*), but our findings suggest that the amplitude of micro-dispersion is primarily related to the sizes of extra-axonal structures independent of the complexity of the major white matter pathway. We also observe that the tortuosity can change between different white matter pathways. Assuming that the local distributions of cell bodies, vessels, and axon fasciculi can generalise within a pathway, then we can expect the micro-dispersion effects on the dMRI signal to be homogeneous.

Notably, high-resolution light-microscopy-techniques such as Polarised Light imaging with in-plane 5 µm and 30-100 µm thick slices (*33*) as well as light-sheet imaging are expected to be too low in resolution to detect the micro-dispersion effects.

Fibre orientation distributions across image resolutions depends on FOV

We found a general agreement in the FODs between the different image modalities and across image resolutions. This is in line with other studies comparing dMRI with structure tensor analysis using both single and multi-fibre models (*34*–*37*).

The FOD discrepancies that we did observe could be attributed to the differences in the FOVs across the imaging modalities. As shown in Fig. 1, we prepared biopsy samples for synchrotron imaging that was on a sufficiently large scale to cover several MRI voxels of isotropic 500 µm size. Indeed, the DESY sample covered multiple MRI voxels, except that a relatively large unstained region in the middle of the sample was not included in the generated FOD. Similarly, the four stacked image volumes of the ESRF measuring 780 µm in length by 210 µm in diameter only covered a fraction of the DESY volume and MRI image voxel. Since the FOD is dependent upon fibre organisation, the observed FOD differences reflect actual anatomical differences, for example with more volumetric weighing in one fibre direction. Therefore, although FODs are independent of image resolution, care must be taken when comparing two modalities without covering the same 3D volume, as observed in the CC (Fig. 3E, F vs. Fig. 3H, I). Examples are validation studies comparing the FOD from diffusion MRI fibre models with that derived from 2D or 3D histology which only rarely cover the same identical volume (*34*, *35*). In cases of differing FOV, there may be a risk of misattributing an actual difference in anatomical information across length scales as a methodological difference.

Tissue micro anisotropy across modalities, image resolutions, and pathology

We show that tissue anisotropy metrics are comparable across modalities but vary with the anatomical length scale. The simple FA metric in the diffusion tensor MRI model was, as expected, sensitive to the average tissue organisation/anisotropy in the voxel. Thus, we found higher anisotropy in the CC (Fig. 2C) as compared to the *centrum semiovale*, a more complex fibre region, much as observed by others (*38*). In contrast, the µFA dMRI metric (*20*, *21*) is sensitive to tissue anisotropy only in micro-domains of 10 µm length scale (molecular displacement). The µFA generates a mean anisotropy value within a voxel, returning similarly high FA values in both the CC and c*entrum semiovale*, thereby confirming the expected independence of FA on the structural organisation (*38*).

In the DESY and ESRF data, anisotropy measured by the structure tensor model is also determined within a micro-domain controlled by the patch-size and produces a distribution

of values from the full volume. We introduced a scale-space parameter that automatically adjusts the patch-size to ensure optimal sensitivity to anisotropic features. Patch-sizes of 18 µm for DESY and 5 µm for ESFR data depict similarly sized micro-domains as in µFA diffusion MR model and were shown to be largely independent of axonal organisation (Fig. 4H and Fig. 7G).

The same anatomical features, namely cell membranes and myelin, dominate the contrast of diffusion vs. structure tensor techniques. In dMRI, these structures are the main sources for restricted and hindered water diffusion, and their osmium staining for the synchrotron scans provides strong image gradients modelled by the structure tensor. However, tissue preparation differs substantially for the two image modalities. In the case of ex vivo MRI, Sun et al. showed that anisotropy of perfusion fixated, hydrated tissue should closely match that in vivo (*39*). However, synchrotron imaging calls for an extra dehydration step before tissue embedding in EPON, which changes the intra- and extracellular volume fractions due to tissue shrinkage (*40*). Similarly, there are shrinkage effects between dehydrated and hydrated synchrotron image samples (*41*). Given the large differences in tissue processing the obtained anisotropy measures naturally differ across the modalities. Nevertheless, as both the diffusion- and structure tensor models were sensitive to the same anatomical features, the observed strong correlation in FA values was expected.

Across image resolutions, the distributions of structure tensor anisotropy also changed, being generally lower and broader in DESY data compared to ESRF data. This could reflect greater partial volume effects in the lower resolution DESY data, thus decreasing the apparent separation of cells and axons. Such image blurring can change the image gradient information used by the structure tensor model, thereby making the anisotropy metric dependent on the image resolution. Therefore, structure tensor quantification of anisotropy metrics calls for invariant image resolution.

In our comparison of structure tensor anisotropy in healthy mice versus cuprizone-induced demyelination, the data clearly shows a lowered anisotropy distribution in focally demyelinated regions compared with healthy WM regions (Fig. 7H). We observed an increased extra-axonal content in the lesion area, thus in agreement with the observed higher density of cells in demyelinated tissue (*42*). By outlining the various cellular structures in 3D, we could visualise what we believe to be cell bodies, macrophages, and the myelin debris engulfed inside macrophages (Fig. 6E).

Interestingly, despite reduced anisotropy in demyelinated regions, the structure tensor still detects a clear directionally dependent anisotropy as in the healthy brain, consistent with the persistence of axons in this animal model despite demyelination (*42*). We did not collect diffusion MRI for the cuprizone-lesioned brains. However, we recently reported relatively preserved µFA values in demyelinated regions of the rat CC (*42*). Similar findings were made in a group of multiple sclerosis patients compared to normal (*38*) supporting our synchrotron anisotropy results.

Limitations

Registration: It was not possible to realise perfect correlational cell-to-cell imaging between the three very different modalities and experimental set-ups. This resulted in minor cross-modal differences between FODs, for example in Fig. 3, where we see a FOD tilt difference due to either misalignment or an anatomical difference, albeit without affecting the interpretation of quantitative measures.

MRI-to-synchrotron registration is challenging due both to the large resolution difference and different contrast mechanisms. Our best option was, therefore, to rely on prior knowledge of fibre orientations to match approximately the samples. Given that we know the site of biopsy sampling, we could confine our search to a small neighbourhood of possible/potential MRI voxels and identify the one giving the best visual match of fibre orientation.

The matching between the different synchrotron volumes was easier and achievable manually for the mouse samples, as they contained large global features in the form of both the CC and cingulum and even a little beyond. Despite our efforts, we could not obtain similar matching for the monkey samples. Due to the imaging at different beamlines, the samples had been physically moved and repositioned in a new setup, thus losing alignment. This process gradually becomes easier and more streamlined as the various synchrotron beamlines develop. Walsh et al. recently succeeded in applying several zoom-ins on a low resolution overview scan of an intact brain within the same scanning session at the ESRF BM05 beamline (*15*). This approach removes the need to collect small selective biopsy samples for the different experiments. However, the finest pixel size in Walsh et al. was isotropic 2.5 µm, which might be too coarse to perform the structure tensor analysis that we undertook to map fibre organisation across anatomical length scales to be compared with diffusion MRI.

Resolution: The different imaging set-ups each have characteristic image resolutions and native voxel sizes, but these are not the only relevant factors in this study. The targeted anatomical features are a primary consideration. Our examination of the monkey and mouse samples at the same beamlines gave approximately the same image resolution, voxel size, and FOV size. Nevertheless, the anatomical scales are quite different simply because the mouse brain is smaller. Thus, the synchrotron FOVs covered only a small part of the CC in the monkey, versus the nearly complete coverage and part of the cingulum bundle in the mouse. Therefore, when defining “high image resolution”, it is essential to relate it to the size of the anatomical structures of interest (*43*).

Additionally, the image resolution does not determine voxel size, since acquired data of fixed resolution can be up- or down-sampled by interpolation. Indeed, interpolation does not change the image information (*43*), while the image resolution is fundamentally defined by the “quality” of the imaging setup. As summarised in Table 2, we interpolated by down sampling for ease of processing and visualisation. Nonetheless, we continue referring to the datasets according to the original reconstructed voxel size (e.g., 75 nm of the ESRF data), as this reflects the approximate inherent image resolution. We minimised the effects of interpolation on the results by specifying the parameters and converting quantities to physical distances whenever possible. Further, we did not target anatomical features such as axon geometries, which cannot be robustly disentangled/quantified after downsampling, although other approaches may serve that purpose (*10*, *12*). Therefore, if the results are to be reproduced by others, then comparable imaging set-ups should be used.

5. MATERIALS AND METHODS

Monkey

The tissue came from a 32-month-old female perfusion-fixated vervet (*Chlorocebus aethiops*) monkey brain, obtained from the Montreal Monkey Brain Bank. The monkey, cared for on the island of St. Kitts, had been treated in line with a protocol approved by The Caribbean Primate Center of St. Kitts.

Mice

C57BL/6 female mice were obtained from Taconic Ltd. (Ry, Denmark). Mice were bred at the Biomedical Laboratory, University of Southern Denmark according to protocols and guidelines approved by the Danish Animal Health Care Committee (2014-15-00369). All animal experiments complied with the EU Directive 2010/63/EU for animal experiments.

Repeated oral administration of the copper chelator bis-cyclohexanone-oxalyldihydrazone (cuprizone) leads to demyelination and oligodendrocyte loss notably in in the CC, and thus serves as a model for the demyelination lesions in patients with multiple sclerosis (MS). Cuprizone (Sigma Aldrich, MO, USA) was administered as 0.4% cuprizone in powdered standard chow to female mice aged 8-9 weeks for five weeks. Control mice were kept on a normal diet. During experiments, mice were weighed every second day to monitor the characteristic weight loss due to cuprizone exposure, with euthanasia of mice losing more than 20% of their baseline body weight. After 5 weeks on cuprizone diet, the mice were euthanized with an overdose of pentobarbital (Glostrup Apotek, Glostrup, Denmark) followed by perfusion with DPB and 4% paraformaldehyde (PFA). The brains were stored in 4% PFA at 4°C.

Diffusion MRI

Two acquisition setups were used to collect the ex vivo diffusion MRI data sets on whole brains from the monkey and mice. The protocol for the monkey brain was from (*10*). Correspondingly, the mouse brain protocol is from (*44*). Note, that the collected mice data from (*44*) have not been included in the synchrotron experiments.

Tissue preparation in both species followed a standard pipeline for diffusion MRI ex vivo (*45*). To reduce susceptibility artefacts and avoid air bubbles, we scanned the monkey brain in a double sealed plastic bag filled with PBS and scanned the mouse brain in a whole. The monkey brain data was collected on an experimental 4.7 Tesla Agilent MRI scanner, whereas the mouse brain data were collected on an experimental 7 Tesla Bruker Biospec MRI scanner. We used a quadrature radio frequency volume coil for the monkey, and a 2-parallel cryo-coil probe for the mouse brains. The isotropic image voxels were 0.55 mm for the monkey brain and 0.125 mm for the mouse. The monkey brain acquisition used an optimised three-shell ActiveAx MRI protocol based on a maximal gradient strength of 300 mT/m for ex vivo tissue as in (*46*). The mice acquisition used a single-shell diffusion MRI protocol for diffusion tensor imaging (*44*). All whole-brain diffusion MRI data sets are available at www.drcmr.map/

Before local fibre modelling, the diffusion MRI datasets were denoised (*47*) and processed in the MRTrix3 software toolbox (RRID: SCR_ 006971)(*10*, *44*) to remove Gibbs ringing artefacts (*48*). Then, we fitted the single-fibre diffusion tensor and the multi-fibre constrained-spherical deconvolution models in the MRTrix3 software toolbox (*23*). For the monkey data, we fitted

the constrained-spherical deconvolution using only a single-shell b-value i.e., 9686 s/mm^2, from which we estimated the fibre orientation distribution (*30*). The diffusion tensors were fitted with a single-shell b-value, i.e., 2957 s/mm^2 for the monkey (*10*) and 4000 s/mm^2 for the mouse (*44*). From the diffusion tensor, we estimated the three Eigenvectors representing fibre orientations as well as the fractional anisotropy (FA) metric (*16*). Since the FA value of microstructure anisotropy is biased by fibre architecture (*10*), we also fitted a micro-tensor model to estimate µFA from the monkey three-shell diffusion MRI data set of monkey (*17*). The diffusion tensor model assumes a single tensor per voxel, whereas the micro-tensor model assumes a micro-tensor regime with many micro-tensors on the diffusion length scale. Hence, the micro-tensor model is not sensitive to fibre organisation (*20*, *21*).

Diffusion MRI human

We used data from four subjects of the Human Connectome Project (HCP) Adult Diffusion database to compute the eigenvalues and eigenvectors of the diffusion tensor (*16*) via a two-step weighted and iterated least-squares method (*49*) as implemented in MRtrix3 (*23*). Data were denoised as indicated in (*50*) using a Rician variance stabilisation transform (*51*) in combination with *PCA* optimal shrinkage (*52*), with subsequent application of Gibbs ringing removal (*48*) and eddy current distortion correction (*53*). For the estimation of the tensor, we selected only the b=0 and the 64 volume-directions corresponding to b=1000s/mm^2. The resulting eigenvector colour-coded maps (*54*) are shown in Figure S1, which is organised similarly to Figure 2A.

Tissue preparation for synchrotron imaging

To perform the SRI experiments, small tissue samples extracted from the monkey and mouse brains were processed and embedded in EPON.

The monkey brain was sliced in the sagittal plane with a monkey brain matrix. Cylindrical samples of 1 mm diameter extracted from the mid sagittal CC and the *centrum semiovale* with a biopsy punch. After post-fixation in 2.5% glutaraldehyde for 24 hours, they were stained by immersion in 0.5% osmium tetroxide (OsO_4), followed by an embedding in EPON resin and shaped into blocks measuring 1 x 1 x 4 mm. For details of sample preparation, see (*10*).

The mouse brains were cut into 1 mm thick coronal slices with a mouse brain matrix. After selecting the slice containing the splenium of the CC, we carefully excised the part of the splenium traversing the mid-sagittal plane and extending approximately 2 mm into the left hemisphere, using a scalpel under a microscope. The mouse brain samples were then processed as described above. Once the EPON resin had polymerized, we used a metallographic grinder to polish the blocks to have a smooth surface, a thickness of approximately 700 µm, and a length of a few millimetres.

Synchrotron imaging

The specimens were imaged at beamline ID16A of the European Synchrotron Radiation Facility (ESRF) with x-ray nano-holotomography, as described in (*10*). In short, the samples were illuminated with a nano-focused cone (*55*) 17 keV x-ray beam. The samples were rotated over 180 degrees, and tomographic scans were acquired at four different propagation distances (*56*). Each scan consisted of 1800 projections with exposure times of 0.22 s, and a pixel size of 100 nm or 75 nm, taking approximately 4 hours to acquire. Upon performing the phase retrieval and tomographic reconstruction, the resulting volumes had dimensions 2048 x 2048 x 2048 voxels. In the case of the healthy mouse sample, the reconstruction was performed in an extended FOV providing a volume of 3200^3 voxels.

The specimens were also imaged at Deutsches Elektronen-Synchrotron (DESY), at the synchrotron radiation nano-CT end station (GINIX) of the P10/PETRA III beamline (*57*). Here, a 13.8 keV x-ray beam illuminated the EPON samples, which were rotated through 180 degrees to acquire tomographic scans at the lens-coupled detector (XSight Micron, Rigaku). Each tomographic scan consisted of 1000 projections with 20 ms of exposure. The detector was placed in the direct-contrast regime of the sample, and a phase retrieval was performed with an in-house Bronnikov-aided correction-based algorithm (*58*, *59*), prior to tomographic reconstruction, which produced volumes of voxel size 550 nm and variable dimensions, as presented in Table 1.

Table 1: Data samples included in this study. All voxel sizes are isotropic.

ID	Specimen	Beamline	Sample	FOV [mm]	Voxel size [nm]
1	Monkey	DESY	Corpus callosum, midbody	0.54 x 0.99 x 0.99	550
2		ESRF		0.21 x 0.21 x 0.21	100
3		ESRF	*Centrum semiovale*	0.21 x 0.21 x 0.21	100
4	Mouse	DESY	Corpus callosum, splenium & cingulum	0.63 x 0.35 x 0.35	550
5		ESRF		0.24 x 0.24 x 0.24	75
6	CPZ Mouse	DESY		0.64 x 0.38 x 0.50	550
7		ESRF		0.30 x 0.30 x 0.30	100

Structure tensor analysis

The primary processing step of the synchrotron volumes entails the computation of the 3D structure tensor in each voxel (*34*, *60*). This involves three steps: (1) Computation of the image gradients, by filtering with the derivative of a Gaussian kernel, where the parameter σ is the standard deviation of the Gaussian; (2) Calculating the outer product of the gradient with itself, yielding a tensor in each image voxel; (3) Aggregation of tensor information local neighbourhood, by filtering with a Gaussian kernel, where the parameter ρ is the standard deviation of the Gaussian.

Similar to Diffusion Tensor MRI (*16*), the eigen-decomposition of the structure tensor defines a 3D ellipsoid, whose axes are scaled according to the eigenvalues λ_1^*, λ_2^* and λ_3^* (where $\lambda_1^* > \lambda_2^* > \lambda_3^*$ and may be normalised to ensure that $\Sigma(\lambda_i^*) = 1$), and their orientations are defined by the three orthogonal eigenvectors $\mathbf{v_1}$, $\mathbf{v_2}$, and $\mathbf{v_3}$. Throughout this paper, the estimated structure tensor decomposition is by default converted to a diffusion-like tensor, as the structure tensor and the diffusion tensor are 'inverted' to one another (*34*). We use the following one parameter (γ) model for converting the eigenvalues:

$$\lambda_i = \exp(-\lambda_i^* / \gamma)$$

Afterwards, the values are normalised to have $\Sigma(\lambda_i) = 1$. The tuning of the (σ,ρ,γ) parameters is done individually for each dataset, as it depends on factors such as the size of the structures of interest and noise in the data. The values are listed in Table 2 for the individual scans.

Scale space structure tensor: The variation of axon diameters within each sample makes it a challenging task to capture all the relevant orientation information with a single set of (σ,ρ)-parameters. Therefore, we employed a 'structure tensor scale space' approach (*61*). Here, the structure tensor is computed (as described above) multiple times using a suite of varying (σ,ρ)-parameters called *scales*. Finally, for each individual voxel we retain just one of the tensors, by finding the *dominant scale* for that voxel. The criterion for selecting the dominant scale is based on the scale-wise relative maximum fractional anisotropy (FA) value.

Let FA_j^i be the calculated FA-value in voxel *j* at scale *i* using the parameter set $(\sigma,\rho)^i$. The dominant scale index, d_j, for voxel *j* is then selected as

$$d_j = argmax_i \left(\frac{FA_j^i}{max_j\left(FA_j^i \right)} \right), \qquad j = 1,2,\ldots,N$$

In other words, at a given scale the maximum observed FA-value across all voxels, $max_j(FA^i{}_j)$, is used as a normalisation factor. In a sense, we are selecting the structure tensor that gives the most anisotropic response across the set of manually pre-defined scales. The use of an FA value for scale selection is reasonable, as we focus on the fibre-like axons. Essentially, we attempt a normalisation, such that derived quantities in each voxel - the eigenvectors, eigenvalues, and FA - are independent of the axon diameter.

Table 2: Structure tensors parameter values used for the samples in this study (see Table 1 for sample ID). The kernel size represents the width of the ρ-kernel converted to physical distance in accordance with the voxel size of the specific dataset.

ID	Voxel size [nm]	Scaling factor	ST-parameters (ρ,σ) [voxels]		ST conversion (γ)	Kernel size [µm]
1	550	2	2.5	0.5	0.30	12
2	100	4	8 scales*	8 scales*	0.30	9.2 - 2
3	100	4	8 scales*	8 scales*	0.30	9.2 - 2
4	550	2	4	1	0.35	18.7
5	75	5	6	1	0.25	9.4
6	550	2	4	1	0.35	18.7

* Scale space structure tensor parameters:
ρ = [5.50, 4.50, 3.50, 3.50, 2.50, 2.50, 1.50, 1.00]
σ = [3.00, 2.75, 2.50, 1.50, 1.50, 1.00, 1.00, 0.50]

Structure tensor based tractography

The principle and the process of structure tensor based tractography are much the same as in diffusion MRI-based tractography, but applied to the synchrotron volumes using the direction vectors of the structure tensor and the deterministic *FACT* algorithm (*23*). The process is controlled by defining **seeding point regions**, **masks** for rejection, inclusion / termination, and various **streamline filtering** parameters, such as minimum length. We utilise an *a priori* anatomical understanding of the sample and it's the axonal organisation to manually generate the seeding region(s). For example, in the CC samples, the axons should primarily run in the L-R direction. We therefore create a mask at the left and right ends of the sample (with some margin from the sample edge). When seeding points in the left region of interest (ROI), streamlines must reach the right ROI to be included, and vice versa.

In several instances, we employed inclusion or rejection masks, which defined the permitted boundaries of travel for the streamlines. In essence, these masks should roughly represent axonal tissue segmentations. Depending on the sample, such a mask can be generated by thresholding either FA - or image intensity values, followed by morphological operations (opening, closing) to close holes and remove small spurious regions.

Streamline Clustering: The output of tractography is unstructured, thus often resulting in an overabundance of streamlines, which may be hard to interpret. It is then beneficial to apply a streamline clustering method, which can collect multiple streamlines into meaningful axonal bundles/fasciculi, while filtering away lone and spurious streamlines. To this end, we used the QuickBundles method (*24*), known for its simplicity and scalability, with manual selection of the distance threshold parameter for each sample individually.

Streamline Analysis: We use two different metrics to quantify the clustered tractography streamlines: Tortuosity and maximum deviation.

The tortuosity index is a single number representing the non-straightness of the trajectory of each streamline. It is calculated as the ratio of the length of a straight line, *d*, (between the streamline endpoints) and the piecewise length of the actual streamline trajectory, *L*.

$$\tau = L / \mathrm{d}$$

The tortuosity index is bound between [1, ∞]. Following this definition, perfectly straight streamlines have a score of 1, and erratic streamlines have higher values. The various tortuosity indices are finally summarised in a histogram for each sample.

The maximum deviation is a supplementary index that describes for each streamline the largest observed physical deviation from a straight line between the given endpoints, which might be described as the maximum amplitude. This index may be easier to interpret in anatomical terms, compared to the unit-less tortuosity.

Similar to the tortuosity measure, we define the direct vector, $\boldsymbol{v}_d$, as going from the streamline starting point to the end point, i.e., $||\boldsymbol{v}_d|| = d$. Additionally, we let $\boldsymbol{v}_i$ be the vector extending from the streamline starting point to either of the *N* streamline sampling points. We then measure the orthogonal distance from each sample point of the streamline to this direct vector by finding the projection of $\mathbf{v}_i$ onto $\mathbf{v}_d$. The maximum deviation, d_{max}, is then defined as the largest observed distance between all sample points and $\mathbf{v}_d$,

$$d_{max} = argmax_i(||v_i - \frac{v_i \cdot v_d}{v_d \cdot v_d} v_d ||) \ , \ i = 2{:}N-1$$

6. ACKNOWLEDGEMENTS

We thank Susanne Sørensen for her assistance with the tissue preparation, and Johanna Perens from Gubra A/S for preparing the mouse MRI data. The authors acknowledge Professor Paul Cumming for critical reading of the manuscript.

We acknowledge DESY (Hamburg, Germany), a member of the Helmholtz Association HGF, for the provision of experimental facilities. Parts of this research were carried out at PETRA III and we would like to thank Dr. Michael Sprung for assistance in using the GINIX setup at P10. Beamtime was allocated for proposal(s) I-20170269 EC and I-20180267 EC.

We acknowledge the European Synchrotron Radiation Facility (ESRF) for provision of synchrotron radiation facilities under proposal numbers LS-2702 and LS-2840 and we would like to thank Peter Cloetens for assistance and support in using beamline ID16A.

M.A. and H.M.K. were supported by Capital Region Research Foundation Grant A5657 (principal investigator: T.B.D.). M.L.E. is grateful for the financial support from Lundbeckfonden (R347-2020-2454). Z.I. is grateful for the financial support from Lundbeckfonden R118-A11472, Scleroseforeningen A41354, and Independent Research Fund Denmark (DFF 9039-00370B). The project has received funding from the European Research Council (ERC) under the European Union's Horizon Europe research and innovation programme (grant agreement No. 101044180) (Principal Investigator: T.B.D.).

The human MRI Data were in part provided by the Human Connectome Project, WU-Minn Consortium (Principal Investigators: David Van Essen and Kamil Ugurbil; 1U54MH091657) funded by the 16 NIH Institutes and Centers that support the NIH Blueprint for Neuroscience Research; and by the McDonnell Center for Systems Neuroscience at Washington University.

7. AUTHOR CONTRIBUTIONS

Conceptualization: T.B.D. **Methodology:** H.M.K., M.A., Y.H., A.P., A.D., M.P., T.S., A.R., M.E., M.T., A.D., M.L., Z.I., M.P., V.A., T.B.D. **Investigation:** H.M.K., M.A., T.B.D., **Visualization:** H.M.K., M.A. **Supervision:** T.B.D. **Writing—original draft:** H.M.K., M.A., T.B.D. **Writing—review and editing:** H.M.K., M.A., Y.H., A.P., A.D., M.P., T.S., A.R., M.E., M.T., A.D., M.L., Z.I., M.P., V.A., T.B.D.

8. REFERENCES

1. K. G. Schilling, F. Rheault, L. Petit, C. B. Hansen, V. Nath, F.-C. Yeh, G. Girard, M. Barakovic, J. Rafael-Patino, T. Yu, E. Fischi-Gomez, M. Pizzolato, M. Ocampo-Pineda, S. Schiavi, E. J. Canales-Rodríguez, A. Daducci, C. Granziera, G. Innocenti, J.-P. Thiran, L. Mancini, S. Wastling, S. Cocozza, M. Petracca, G. Pontillo, M. Mancini, S. B. Vos, V. N. Vakharia, J. S. Duncan, H. Melero, L. Manzanedo, E. Sanz-Morales, Á. Peña-Melián, F. Calamante, A. Attyé, R. P. Cabeen, L. Korobova, A. W. Toga, A. A. Vijayakumari, D. Parker, R. Verma, A. Radwan, S. Sunaert, L. Emsell, A. De Luca, A. Leemans, C. J. Bajada, H. Haroon, H. Azadbakht, M. Chamberland, S. Genc, C. M. W. Tax, P.-H. Yeh, R. Srikanchana, C. D. Mcknight, J. Y.-M. Yang, J. Chen, C. E. Kelly, C.-H. Yeh, J. Cochereau, J. J. Maller, T. Welton, F. Almairac, K. K. Seunarine, C. A. Clark, F. Zhang, N. Makris, A. Golby, Y. Rathi, L. J. O'Donnell, Y. Xia, D. B. Aydogan, Y. Shi, F. G. Fernandes, M. Raemaekers, S. Warrington, S. Michielse, A. Ramírez-Manzanares, L. Concha, R. Aranda, M. R. Meraz, G. Lerma-Usabiaga, L. Roitman, L. S. Fekonja, N. Calarco, M. Joseph, H. Nakua, A. N. Voineskos, P. Karan, G. Grenier, J. H. Legarreta, N. Adluru, V. A. Nair, V. Prabhakaran, A. L. Alexander, K. Kamagata, Y. Saito, W. Uchida, C. Andica, M. Abe, R. G. Bayrak, C. A. M. G. Wheeler-Kingshott, E. D'Angelo, F. Palesi, G. Savini, N. Rolandi, P. Guevara, J. Houenou, N. López-López, J.-F. Mangin, C. Poupon, C. Román, A. Vázquez, C. Maffei, M. Arantes, J. P. Andrade, S. M. Silva, V. D. Calhoun, E. Caverzasi, S. Sacco, M. Lauricella, F. Pestilli, D. Bullock, Y. Zhan, E. Brignoni-Perez, C. Lebel, J. E. Reynolds, I. Nestrasil, R. Labounek, C. Lenglet, A. Paulson, S. Aulicka, S. R. Heilbronner, K. Heuer, B. Q. Chandio, J. Guaje, W. Tang, E. Garyfallidis, R. Raja, A. W. Anderson, B. A. Landman, M. Descoteaux, Tractography dissection variability: What happens when 42 groups dissect 14 white matter bundles on the same dataset? *Neuroimage*. **243**, 118502 (2021).

2. S. Sarubbo, L. Petit, A. De Benedictis, F. Chioffi, M. Ptito, T. B. Dyrby, Uncovering the inferior fronto-occipital fascicle and its topological organization in non-human primates: the missing connection for language evolution. *Brain Struct. Funct.* **224**, 1553–1567 (2019).

3. M. Sach, G. Winkler, V. Glauche, J. Liepert, B. Heimbach, M. A. Koch, C. Büchel, C. Weiller, Diffusion tensor MRI of early upper motor neuron involvement in amyotrophic lateral sclerosis. *Brain*. **127**, 340–350 (2004).

4. V. J. Wedeen, D. L. Rosene, R. Wang, G. Dai, F. Mortazavi, P. Hagmann, J. H. Kaas, W.-Y. I. Tseng, The geometric structure of the brain fiber pathways. *Science*. **335**, 1628–1634 (2012).

5. M. Catani, I. Bodi, F. Dell'Acqua, Comment on "The geometric structure of the brain fiber pathways." *Science*. **337** (2012), p. 1605.

6. K. H. Maier-Hein, P. F. Neher, J.-C. Houde, M.-A. Côté, E. Garyfallidis, J. Zhong, M. Chamberland, F.-C. Yeh, Y.-C. Lin, Q. Ji, W. E. Reddick, J. O. Glass, D. Q. Chen, Y. Feng, C. Gao, Y. Wu, J. Ma, R. He, Q. Li, C.-F. Westin, S. Deslauriers-Gauthier, J. O. O. González, M. Paquette, S. St-Jean, G. Girard, F. Rheault, J. Sidhu, C. M. W. Tax, F. Guo, H. Y. Mesri, S. Dávid, M. Froeling, A. M. Heemskerk, A. Leemans, A. Boré, B. Pinsard, C. Bedetti, M. Desrosiers, S. Brambati, J. Doyon, A. Sarica, R. Vasta, A. Cerasa, A. Quattrone, J. Yeatman, A. R. Khan, W. Hodges, S. Alexander, D. Romascano, M. Barakovic, A. Auría, O. Esteban, A. Lemkaddem, J.-P. Thiran, H. E. Cetingul, B. L. Odry, B. Mailhe, M. S. Nadar, F. Pizzagalli, G. Prasad, J. E. Villalon-Reina, J. Galvis, P. M. Thompson, F. D. S. Requejo, P. L. Laguna, L. M. Lacerda, R. Barrett, F. Dell'Acqua, M. Catani, L. Petit, E. Caruyer, A. Daducci, T. B. Dyrby, T. Holland-Letz, C. C. Hilgetag, B. Stieltjes, M. Descoteaux, The challenge of mapping the human connectome based on diffusion tractography. *Nat. Commun.* **8**, 1349 (2017).

7. K. Schilling, Y. Gao, V. Janve, I. Stepniewska, B. A. Landman, A. W. Anderson, Can increased spatial resolution solve the crossing fiber problem for diffusion MRI? *NMR Biomed.* **30** (2017), doi:10.1002/nbm.3787.

8. D. C. Alexander, T. B. Dyrby, M. Nilsson, H. Zhang, Imaging brain microstructure with diffusion MRI: practicality and applications. *NMR Biomed.* **32**, e3841 (2019).

9. S. Trinkle, S. Foxley, N. Kasthuri, P. La Rivière, Synchrotron X-ray micro-CT as a validation dataset for diffusion MRI in whole mouse brain. *Magn. Reson. Med.* **86**, 1067–1076 (2021).

10. M. Andersson, H. M. Kjer, J. Rafael-Patino, A. Pacureanu, B. Pakkenberg, J.-P. Thiran, M. Ptito, M. Bech, A. Bjorholm Dahl, V. Andersen Dahl, T. B. Dyrby, Axon morphology is modulated by the local environment and impacts the noninvasive investigation of its structure-function relationship. *Proc. Natl. Acad. Sci. U. S. A.* **117**, 33649–33659 (2020).

11. H.-H. Lee, S. N. Jespersen, E. Fieremans, D. S. Novikov, The impact of realistic axonal shape on axon diameter estimation using diffusion MRI. *Neuroimage*. **223**, 117228 (2020).

12. M. Andersson, M. Pizzolato, H. M. Kjer, Katrine Forum Skodborg, H. Lundell, T. B. Dyrby, Does powder averaging remove dispersion bias in diffusion MRI diameter estimates within real 3D axonal architectures? *NeuroImage*. **248**, 118718 (2022).

13. F. Mortazavi, A. L. Oblak, W. Z. Morrison, J. D. Schmahmann, H. E. Stanley, V. J. Wedeen, D. L. Rosene, Geometric Navigation of Axons in a Cerebral Pathway: Comparing dMRI with Tract Tracing and Immunohistochemistry. *Cereb. Cortex*. **28**, 1219–1232 (2018).

14. J. Zhou, Y. Wen, L. She, Y.-N. Sui, L. Liu, L. J. Richards, M.-M. Poo, Axon position within the corpus callosum determines contralateral cortical projection. *Proc. Natl. Acad. Sci. U. S. A.* **110**, E2714–23 (2013).

15. C. L. Walsh, P. Tafforeau, W. L. Wagner, D. J. Jafree, A. Bellier, C. Werlein, M. P. Kühnel, E. Boller, S. Walker-Samuel, J. L. Robertus, D. A. Long, J. Jacob, S. Marussi, E. Brown, N. Holroyd, D. D. Jonigk, M. Ackermann, P. D. Lee, Imaging intact human organs with local resolution of cellular structures using hierarchical phase-contrast tomography. *Nat. Methods*. **18**, 1532–1541 (2021).

16. P. J. Basser, J. Mattiello, D. LeBihan, MR diffusion tensor spectroscopy and imaging. *Biophys. J.* **66**, 259–267 (1994).

17. E. Kaden, N. D. Kelm, R. P. Carson, M. D. Does, D. C. Alexander, Multi-compartment microscopic diffusion imaging. *Neuroimage*. **139**, 346–359 (2016).

18. J.-D. Tournier, F. Calamante, A. Connelly, Robust determination of the fibre orientation distribution in diffusion MRI: non-negativity constrained super-resolved spherical deconvolution. *Neuroimage*. **35**, 1459–1472 (2007).

19. P. J. Basser, C. Pierpaoli, Microstructural and physiological features of tissues elucidated by quantitative-diffusion-tensor MRI. *J. Magn. Reson. B*. **111**, 209–219 (1996).

20. S. Lasič, F. Szczepankiewicz, S. Eriksson, M. Nilsson, D. Topgaard, Microanisotropy imaging: quantification of microscopic diffusion anisotropy and orientational order parameter by diffusion MRI with magic-angle spinning of the q-vector. *Front. Phys.* **2** (2014), doi:10.3389/fphy.2014.00011.

21. S. N. Jespersen, H. Lundell, C. K. Sønderby, T. B. Dyrby, Orientationally invariant metrics of apparent compartment eccentricity from double pulsed field gradient diffusion experiments. *NMR Biomed.* **26**, 1647–1662 (2013).

22. J. Schmahmann, D. Pandya, *Fiber Pathways of the Brain* (Oxford University Press, USA, 2009).

23. J.-D. Tournier, R. Smith, D. Raffelt, R. Tabbara, T. Dhollander, M. Pietsch, D. Christiaens, B. Jeurissen, C.-H. Yeh, A. Connelly, MRtrix3: A fast, flexible and open software framework for medical image processing and visualisation. *Neuroimage*. **202**, 116137 (2019).

24. E. Garyfallidis, M. Brett, M. M. Correia, G. B. Williams, I. Nimmo-Smith, QuickBundles, a Method for Tractography Simplification. *Front. Neurosci.* **6**, 175 (2012).

25. M. Nilsson, J. Lätt, F. Ståhlberg, D. van Westen, H. Hagslätt, The importance of axonal undulation in diffusion MR measurements: a Monte Carlo simulation study. *NMR Biomed.* **25**, 795–805 (2012).

26. R. Caminiti, H. Ghaziri, R. Galuske, P. R. Hof, G. M. Innocenti, Evolution amplified processing with temporally dispersed slow neuronal connectivity in primates. *Proc. Natl. Acad. Sci. U. S. A.* **106**, 19551–19556 (2009).

27. A. F. D. Howard, I. N. Huszar, A. Smart, M. Cottaar, G. Daubney, T. Hanayik, A. A. Khrapitchev, R. B. Mars, J. Mollink, C. Scott, N. R. Sibson, J. Sallet, S. Jbabdi, K. L. Miller, An open resource combining multi-contrast MRI and microscopy in the macaque brain. *Nat. Commun.* **14**, 4320 (2023).

28. J. Mollink, M. Kleinnijenhuis, A.-M. van Cappellen van Walsum, S. N. Sotiropoulos, M. Cottaar, C. Mirfin, M. P. Heinrich, M. Jenkinson, M. Pallebage-Gamarallage, O. Ansorge, S. Jbabdi, K. L. Miller, Evaluating fibre orientation dispersion in white matter: Comparison of diffusion MRI, histology and polarized light imaging. *Neuroimage*. **157**, 561–574 (2017).

29. C. M. W. Tax, T. Dela Haije, A. Fuster, C.-F. Westin, M. A. Viergever, L. Florack, A. Leemans, Sheet Probability Index (SPI): Characterizing the geometrical organization of the white matter with diffusion MRI. *Neuroimage*. **142**, 260–279 (2016).

30. J.-D. Tournier, F. Calamante, D. G. Gadian, A. Connelly, Direct estimation of the fiber orientation density function from diffusion-weighted MRI data using spherical deconvolution. *Neuroimage*. **23**, 1176–1185 (2004).

31. J. Pingel, H. M. Kjer, F. Biering-Sørensen, R. Feidenhans'l, T. B. Dyrby, 3D synchrotron imaging of muscle tissues at different atrophic stages in stroke and spinal cord injury: a proof-of-concept study. *Sci. Rep.* **12**, 17289 (2022).

32. H.-H. Lee, K. Yaros, J. Veraart, J. L. Pathan, F.-X. Liang, S. G. Kim, D. S. Novikov, E. Fieremans, Along-axon diameter variation and axonal orientation dispersion revealed with 3D electron microscopy: implications for quantifying brain white matter microstructure with histology and diffusion MRI. *Brain Struct. Funct.* **224**, 1469–1488 (2019).

33. M. Axer, K. Amunts, D. Grässel, C. Palm, J. Dammers, H. Axer, U. Pietrzyk, K. Zilles, A novel approach to the human connectome: ultra-high resolution mapping of fiber tracts in the brain. *Neuroimage*. **54**, 1091–1101 (2011).

34. A. R. Khan, A. Cornea, L. A. Leigland, S. G. Kohama, S. N. Jespersen, C. D. Kroenke, 3D structure tensor analysis of light microscopy data for validating diffusion MRI. *Neuroimage*. **111**, 192–203 (2015).

35. M. D. Budde, J. A. Frank, Examining brain microstructure using structure tensor analysis of histological sections. *Neuroimage*. **63**, 1–10 (2012).

36. C. Leuze, M. Goubran, M. Barakovic, M. Aswendt, Q. Tian, B. Hsueh, A. Crow, E. M. M. Weber, G. K. Steinberg, M. Zeineh, E. D. Plowey, A. Daducci, G. Innocenti, J.-P. Thiran, K. Deisseroth, J. A. McNab, Comparison of diffusion MRI and CLARITY fiber orientation estimates in both gray and white matter regions of human and primate brain. *Neuroimage*. **228**, 117692 (2021).

37. K. Schilling, V. Janve, Y. Gao, I. Stepniewska, B. A. Landman, A. W. Anderson, Comparison of 3D orientation distribution functions measured with confocal microscopy and diffusion MRI. *Neuroimage*. **129**, 185–197 (2016).

38. K. W. Andersen, S. Lasič, H. Lundell, M. Nilsson, D. Topgaard, F. Sellebjerg, F. Szczepankiewicz, H. R. Siebner, M. Blinkenberg, T. B. Dyrby, Disentangling white-matter damage from physiological fibre orientation dispersion in multiple sclerosis. *Brain Commun*. **2**, fcaa077 (2020).

39. S.-W. Sun, J. J. Neil, H.-F. Liang, Y. Y. He, R. E. Schmidt, C. Y. Hsu, S.-K. Song, Formalin fixation alters water diffusion coefficient magnitude but not anisotropy in infarcted brain. *Magn. Reson. Med.* **53**, 1447–1451 (2005).

40. N. Korogod, C. C. H. Petersen, G. W. Knott, Ultrastructural analysis of adult mouse neocortex comparing aldehyde perfusion with cryo fixation. *Elife*. **4** (2015), doi:10.7554/eLife.05793.

41. M. Töpperwien, A. Markus, F. Alves, T. Salditt, Contrast enhancement for visualizing neuronal cytoarchitecture by propagation-based x-ray phase-contrast tomography. *Neuroimage*. **199**, 70–80 (2019).

42. Y. He, S. Aznar, H. R. Siebner, T. B. Dyrby, In vivo tensor-valued diffusion MRI of focal demyelination in white and deep grey matter of rodents. *Neuroimage Clin*. **30**, 102675 (2021).

43. T. B. Dyrby, H. Lundell, M. W. Burke, N. L. Reislev, O. B. Paulson, M. Ptito, H. R. Siebner, Interpolation of diffusion weighted imaging datasets. *Neuroimage*. **103**, 202–213 (2014).

44. J. Perens, C. G. Salinas, U. Roostalu, J. L. Skytte, C. Gundlach, J. Hecksher-Sørensen, A. B. Dahl, T. B. Dyrby, Multimodal 3D Mouse Brain Atlas Framework with the Skull-Derived Coordinate System. *Neuroinformatics*. **21**, 269–286 (2023).

45. T. B. Dyrby, W. F. C. Baaré, D. C. Alexander, J. Jelsing, E. Garde, L. V. Søgaard, An ex vivo imaging pipeline for producing high-quality and high-resolution diffusion-weighted imaging datasets. *Hum. Brain Mapp.* **32**, 544–563 (2011).

46. T. B. Dyrby, L. V. Sogaard, M. G. Hall, M. Ptito, D. C. Alexander, Contrast and stability of the axon diameter index from microstructure imaging with diffusion MRI. *Magn. Reson. Med.* **70**, 711–721 (2013).

47. J. Veraart, E. Fieremans, D. S. Novikov, Diffusion MRI noise mapping using random matrix theory. *Magn. Reson. Med.* **76**, 1582–1593 (2016).

48. E. Kellner, B. Dhital, V. G. Kiselev, M. Reisert, Gibbs-ringing artifact removal based on local subvoxel-shifts. *Magnetic Resonance in Medicine*. **76** (2016), pp. 1574–1581.

49. J. Veraart, J. Sijbers, S. Sunaert, A. Leemans, B. Jeurissen, Weighted linear least squares estimation of diffusion MRI parameters: strengths, limitations, and pitfalls. *Neuroimage*. **81**, 335–346 (2013).

50. M. Pizzolato, E. J. Canales-Rodríguez, M. Andersson, T. B. Dyrby, Axial and radial axonal diffusivities and radii from single encoding strongly diffusion-weighted MRI. *Med. Image Anal.* **86**, 102767 (2023).

51. A. Foi, "Noise estimation and removal in MR imaging: The variance-stabilization approach" in *2011 IEEE International Symposium on Biomedical Imaging: From Nano to Macro* (2011), pp. 1809–1814.

52. M. Gavish, D. L. Donoho, Optimal Shrinkage of Singular Values. *IEEE Trans. Inf. Theory*. **63**, 2137–2152 (2017).

53. J. L. R. Andersson, S. N. Sotiropoulos, An integrated approach to correction for off-resonance effects and subject movement in diffusion MR imaging. *Neuroimage*. **125**, 1063–1078 (2016).

54. S. Pajevic, C. Pierpaoli, Color schemes to represent the orientation of anisotropic tissues from diffusion tensor data: application to white matter fiber tract mapping in the human brain. *Magn. Reson. Med.* **43**, 921 (2000).

55. J. C. Da Silva, A. Pacureanu, Y. Yang, S. Bohic, C. Morawe, R. Barrett, P. Cloetens, Efficient concentration of high-energy x-rays for diffraction-limited imaging resolution. *Optica*. **4**, 492–495 (2017).

56. M. Hubert, A. Pacureanu, C. Guilloud, Y. Yang, J. C. da Silva, J. Laurencin, F. Lefebvre-Joud, P. Cloetens, Efficient correction of wavefront inhomogeneities in X-ray holographic nanotomography by random sample displacement. *Appl. Phys. Lett.* **112** (2018) (available at https://pubs.aip.org/aip/apl/article/112/20/203704/236285).

57. T. Salditt, M. Osterhoff, M. Krenkel, R. N. Wilke, M. Priebe, M. Bartels, S. Kalbfleisch, M. Sprung, Compound focusing mirror and X-ray waveguide optics for coherent imaging

and nano-diffraction. *J. Synchrotron Radiat.* **22**, 867–878 (2015).

58. L. M. Lohse, A. L. Robisch, M. Töpperwien, S. Maretzke, M. Krenkel, J. Hagemann, T. Salditt, A phase-retrieval toolbox for X-ray holography and tomography. *J. Synchrotron Radiat.* **27**, 852–859 (2020).

59. Y. De Witte, M. Boone, J. Vlassenbroeck, M. Dierick, L. Van Hoorebeke, Bronnikov-aided correction for x-ray computed tomography. *J. Opt. Soc. Am. A Opt. Image Sci. Vis.* **26**, 890–894 (2009).

60. N. Jeppesen, L. P. Mikkelsen, A. B. Dahl, A. N. Christensen, V. A. Dahl, Quantifying effects of manufacturing methods on fiber orientation in unidirectional composites using structure tensor analysis. *Compos. Part A Appl. Sci. Manuf.* **149**, 106541 (2021).

61. T. Lindeberg, Feature Detection with Automatic Scale Selection. *Int. J. Comput. Vis.* **30**, 79–116 (1998).

9. SUPPLEMENTARY

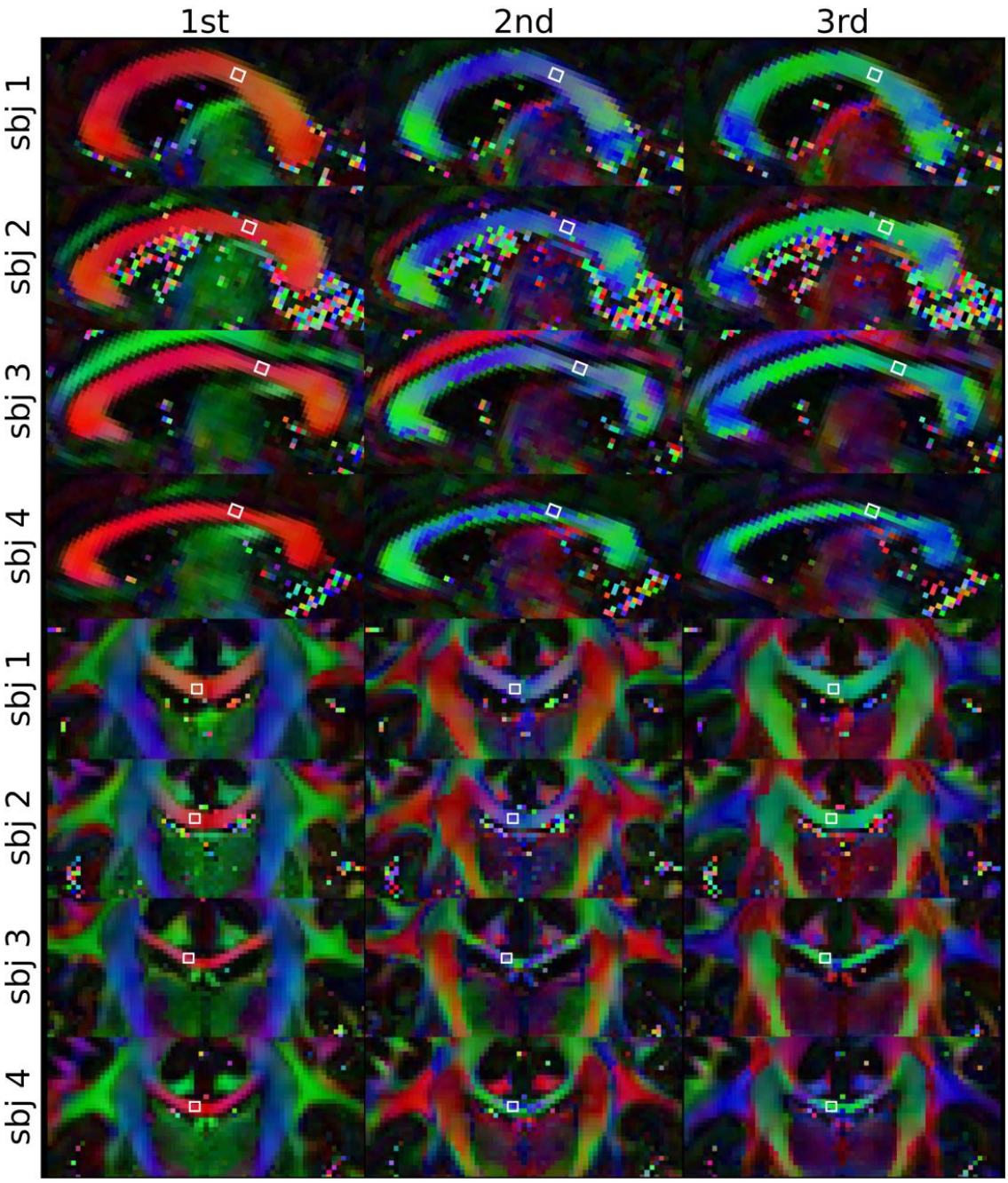

Figure S1: HCP dataset diffusion tensor modelling. The RGB colour-coded first, second, and third eigenvectors (ordered by decreasing eigenvalues) for the four subjects in both sagittal and coronal crop-out views.